

17026

APPENDIX III

THE AERODYNAMICS OF ACTRON

by

A. J. Baker, Ph.D.  
University of Tennessee  
Knoxville, Tennessee

and

PREDICTION OF SECONDARY VORTEX FLOWFIELDS:  
INDUCED BY MULTIPLE FREE-JETS  
ISSUING IN CLOSE PROXIMITY

by

A. J. Baker, Ph.D.  
University of Tennessee  
Knoxville, Tennessee

J. A. Orzechowski, Ph.D.,  
Computational Mechanics Consultants, Inc.  
Knoxville, Tennessee

G. E. Stungis, Ph.D.,  
Brown & Williamson Tobacco Corporation  
Louisville, Kentucky

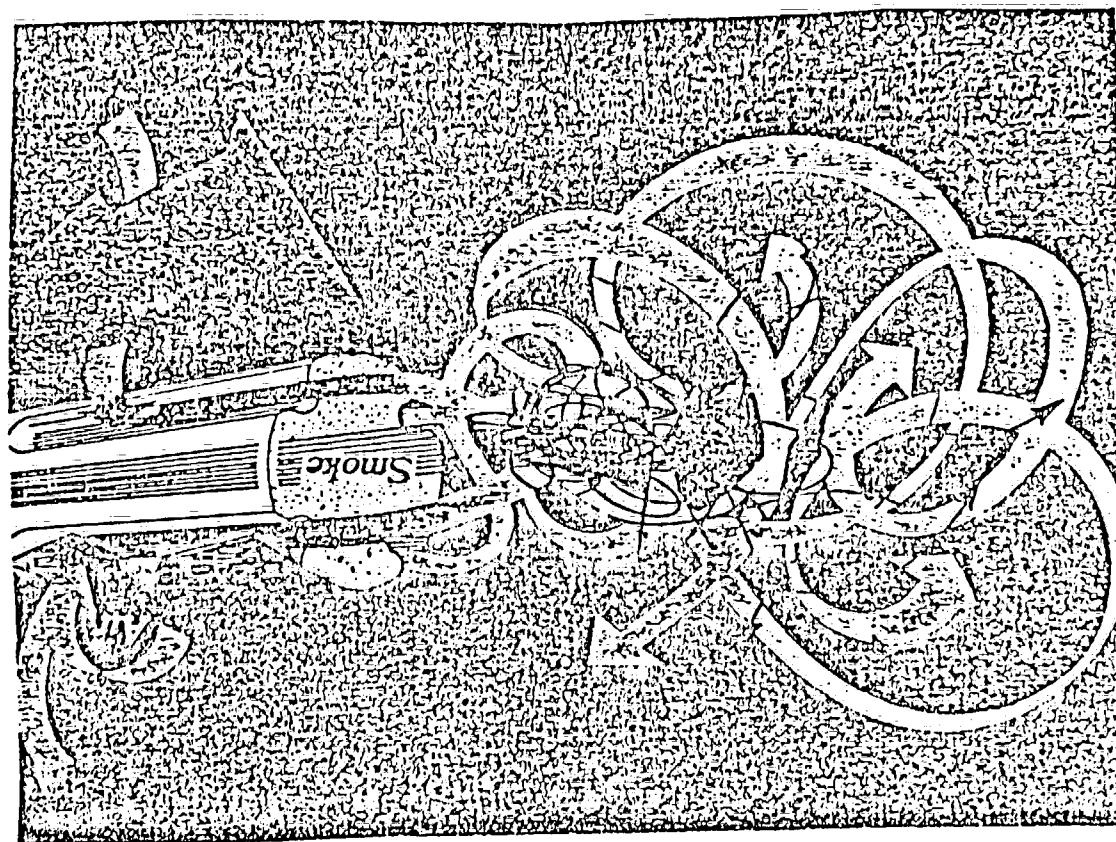
DRAFT  
COMMERCIAL IN CONFIDENCE

1005062847

THE  
AERODYNAMICS  
OF ACTRON  
—  
THEORETICAL ANALYSIS

1005062848

1005062849



VISUALIZATION OF ACTRON FLOWFIELD

## THEORETICAL ANALYSIS

### BASIC IDENTIFICATIONS

- DIFFERENTIAL EQUATION SYSTEM
- TURBULENCE CLOSURE
- NUMERICAL SOLUTION ALGORITHM
- VERIFICATION TESTS

### ANALYSIS SPECIFICATIONS

- SOLUTION DOMAIN
- BOUNDARY CONDITIONS
- INITIAL CONDITIONS
- CLOSURE MODEL CONSTANTS

1005062850

## DIFFERENTIAL EQUATIONS

### CONTINUITY, MOMENTUM AND ENERGY

- FIRST ORDER EFFECTS

DOWNSTREAM DIFFUSION NEGLIGIBLE

TRANSVERSE MOMENTA GOVERNS PRESSURE

CONTINUITY GOVERNS TRANSVERSE VELOCITIES

- REYNOLDS STRESS COMPONENTS OF EQUAL ORDER

- WELL - POSED PROBLEM STATEMENT REQUIRED

### TURBULENCE CLOSURE

- TKE - EPSILON TWO-EQUATION SYSTEM

- REYNOLDS STRESS CONSTITUTIVE MODEL

1005062851

# TURBULENT THREE-DIMENSIONAL AERODYNAMIC FLOW

## 3D THIN LAYER NAVIER-STOKES EQUATIONS ( $1 \leq i \leq 3$ ) ( $2 \leq l \leq 3$ )

$$L(\phi) = \text{CONVECTION} + \text{SOURCE} + \text{DIFFUSION} + \text{SINK} = 0$$

$$L(\bar{\rho}) = \frac{\partial}{\partial x_i} (\bar{\rho} \tilde{u}_i) = 0$$

$$L(\tilde{u}_1) = \frac{\partial}{\partial x_i} (\bar{\rho} \tilde{u}_i \tilde{u}_1) + \frac{\partial \bar{p}}{\partial x_1} - \frac{\partial}{\partial x_l} \left[ \frac{\mu}{\text{Re}} \frac{\partial \tilde{u}_1}{\partial x_l} - \overline{\rho u_1' u_l'} \right] = 0$$

$$L(\tilde{u}_2) = \frac{\partial}{\partial x_i} (\bar{\rho} \tilde{u}_i \tilde{u}_2) + \frac{\partial \bar{p}}{\partial x_2} - \frac{\partial}{\partial x_l} \left[ \frac{\mu}{\text{Re}} \left( \frac{\partial \tilde{u}_2}{\partial x_l} + \frac{\partial \tilde{u}_l}{\partial x_2} \right) - \overline{\rho u_2' u_l'} \right] = 0$$

$$L(\tilde{u}_3) = \frac{\partial}{\partial x_i} (\bar{\rho} \tilde{u}_i \tilde{u}_3) + \frac{\partial \bar{p}}{\partial x_3} - \frac{\partial}{\partial x_l} \left[ \frac{\mu}{\text{Re}} \left( \frac{\partial \tilde{u}_3}{\partial x_l} + \frac{\partial \tilde{u}_l}{\partial x_3} \right) - \overline{\rho u_3' u_l'} \right] = 0$$

$$L(k) = \frac{\partial}{\partial x_i} (\bar{\rho} \tilde{u}_i k) + \overline{\rho u_i' u_l'} \frac{\partial \tilde{u}_i}{\partial x_l} - \frac{\partial}{\partial x_l} \left[ \frac{\mu}{\text{Re}} + \bar{\rho} C_k \frac{k}{\epsilon} \overline{u_i' u_l'} \frac{\partial k}{\partial x_l} \right] + \bar{\rho} \epsilon = 0$$

$$L(\epsilon) = \frac{\partial}{\partial x_i} (\bar{\rho} \tilde{u}_i \epsilon) + C_1 \overline{\rho u_i' u_l'} \frac{\epsilon}{k} \frac{\partial \tilde{u}_i}{\partial x_l} - \frac{\partial}{\partial x_l} \left[ \bar{\rho} C_\epsilon \frac{k}{\epsilon} \overline{u_i' u_l'} \frac{\partial \epsilon}{\partial x_l} \right] + C_2 \frac{\epsilon^2}{k} = 0$$

1005062852

# REYNOLDS STRESS CLOSURE MODEL

FROM CONTINUUM MECHANICS:

$$\overline{u_i' u_j'} = \alpha_1 \delta_{ij} + \alpha_2 E_{ij} + \alpha_3 E_{ik} E_{kj} + \dots, \quad E_{ij} = \left[ \frac{\partial \tilde{u}_i}{\partial x_j} + \frac{\partial \tilde{u}_j}{\partial x_i} \right]$$

PARABOLIZED PLUS 2<sup>ND</sup> ORDER:

$$\begin{aligned} \overline{u_1' u_1'} &= C_1 k - 2C_1 \frac{k^2}{\epsilon} \frac{\partial \tilde{u}_1}{\partial x_1} - C_2 \frac{k}{\epsilon} C_4 \frac{k^2}{\epsilon} \left[ \frac{\partial \tilde{u}_1}{\partial x_2} \frac{\partial \tilde{u}_1}{\partial x_2} \right] \\ \overline{u_2' u_2'} &= C_3 k - 2C_1 \frac{k^2}{\epsilon} \frac{\partial \tilde{u}_2}{\partial x_2} - C_2 \frac{k}{\epsilon} C_4 \frac{k^2}{\epsilon} \left[ \frac{\partial \tilde{u}_1}{\partial x_2} \frac{\partial \tilde{u}_1}{\partial x_2} \right] \\ \overline{u_3' u_3'} &= C_3 k - 2C_1 \frac{k^2}{\epsilon} \frac{\partial \tilde{u}_3}{\partial x_3} - C_2 \frac{k}{\epsilon} C_4 \frac{k^2}{\epsilon} \left[ \frac{\partial \tilde{u}_1}{\partial x_2} \frac{\partial \tilde{u}_1}{\partial x_2} \right] \\ \overline{u_1' u_2'} &= - C_4 \frac{k^2}{\epsilon} \frac{\partial \tilde{u}_1}{\partial x_2} \\ \overline{u_1' u_3'} &= - C_4 \frac{k^2}{\epsilon} \frac{\partial \tilde{u}_1}{\partial x_3} \\ \overline{u_2' u_3'} &= - C_4 \frac{k^2}{\epsilon} \left[ \frac{\partial \tilde{u}_2}{\partial x_3} + \frac{\partial \tilde{u}_3}{\partial x_2} \right] - C_2 \frac{k}{\epsilon} C_4 \frac{k^2}{\epsilon} \left[ \frac{\partial \tilde{u}_1}{\partial x_2} \frac{\partial \tilde{u}_1}{\partial x_3} \right] \end{aligned}$$

1005062853

## THREE - DIMENSIONAL DIRECTED FLOWFIELDS

### PARABOLIC ALGORITHM STRUCTURES

#### CONTINUITY:

- PSEUDO - PRESSURE CORRECTION  
SPALDING ET. AL. (1970 - 78)
- POTENTIAL FUNCTION / AXIAL VORTICITY  
BRILEY ET. AL. (1974 - 80),  
GHIA (1974 - 76), DODGE (1976 - 80)
- PENALTY DIFFERENTIAL CONSTRAINT  
BAKER ET. AL. (1979 - 81)

#### PRESSURE:

- AXIAL MASS - CONSERVING GRADIENT  
"PARTIALLY - PARABOLIC"
- INVISCID POISSON EQUATION  
WALL MODIFICATIONS
- ORDERED POISSON EQUATION  
COMPLEMENTARY SOLUTION (3D POTENTIAL FLOW)  
PARTICULAR SOLUTION (TURBULENCE + CONVECTION)

1005062854



TWO - DIMENSIONAL PARABOLIC NAVIER - STOKES  
STEADY, UNIDIRECTIONAL TURBULENT FLOWS  
FINITE ELEMENT PENALTY ALGORITHM

FORMULATIONAL STRUCTURE FROM CLASSICAL VARIATIONAL CONCEPTS :

$$\begin{aligned} I(\bar{u}_p^h, \bar{v}_p^h, \lambda_p) &= \int_{\Omega} f(\bar{u}_p^h) + \frac{1}{2} \lambda_p \int_{\Omega} (\nabla \cdot \bar{u}_p^h)^2 \\ &= \frac{1}{2Re} (\nabla \bar{u}_p^h)^2 + \dots \end{aligned}$$

WEIGHTED RESIDUALS GALERKIN ALGORITHM :

$$\begin{aligned} \bar{u}_p^h &\equiv \bigcup_e \bar{u}_e^e(x, y) = \bigcup_e \left[ \{N_k(y)\}^T \{QI(x)\}_e \right] \\ \int_{R^1} \{N_k\} L^\delta(\bar{v}^h) - \frac{\lambda}{2} \int_{R^1} \nabla \{N_k\} L^1(\bar{p}_o^h) &\equiv \{0\} \\ \int_{R^1} \{N_k\} L^1(\bar{u}^h, k^h, \epsilon^h, \bar{v}^h) &\equiv \{0\} \end{aligned}$$

1005062855

TWO - DIMENSIONAL PARABOLIC NAVIER - STOKES  
STEADY, UNIDIRECTIONAL TURBULENT FLOWS  
FINITE ELEMENT PENALTY ALGORITHM

PENALTY FUNCTION FORM :

$$\begin{aligned} L^1(\bar{p}_o^h) &= \nabla \cdot \vec{u}^h \neq 0 \\ &\equiv \nabla^2 \phi_p^h \end{aligned}$$

BOUNDARY CONDITIONS ON  $\phi_p^h$  :

- POROUS - DIRICHLET
- NON - POROUS - NEUMANN

$$\nabla \phi^h \cdot \hat{n} = \vec{u}^h \cdot \hat{n} = 0$$

PENALTY PARAMETER :

$$\lambda_p \Rightarrow C \Delta x [U_p(x_1, x_2)]$$

1005062856

# 3DPNS FINITE ELEMENT PENALTY CONSTRAINT ALGORITHM

## FINITE ELEMENT SOLUTION ALGORITHM:

- SEMI - DISCRETE APPROXIMATION ON  $R^3$ :

$$q_{\alpha}^h(x_1, x_1) \equiv \sum_e \{N_k(x_1)\}^T \{QI(x_1)\}_e$$

- APPROXIMATION ERROR EXTREMIZATION:

$$\int_{R^2} \{N\} L(q_{\alpha}^h) + \oint_{\partial R} \{N\} l(q_{\alpha}^h) \equiv \{0\}$$

- TRANSVERSE MOMENTUM CONTINUITY CONSTRAINT:

$$\int_{R^2} \{N\} L(u_1^h) + \vec{\lambda} \cdot \int_{R^2} \nabla \{N\} L(\rho^h) \equiv \{0\}$$

- IMPLICIT INTEGRATION ON  $X_1$

$$\{FI\} \equiv \{QI\}_{j+1} - \{QI\}_j - \Delta x_1 \{QI\}_{j+1/2}' \equiv \{0\}$$

1005062857

### 3D PARABOLIC NAVIER-STOKES EQUATIONS

#### SPACE MARCHING :

- $\tilde{U}_1, k, e, \tilde{H}$
- $\tilde{U}_2, \tilde{U}_3$  ( CONSTRAINED S.T.  $\nabla \cdot \tilde{U} = 0$  )

#### POISSON EQUATIONS :

- PRESSURE (  $P_C + P_P$  )
- CONTINUITY FUNCTION

#### ALGEBRAIC :

- EQUATION OF STATE
- REYNOLDS STRESSES

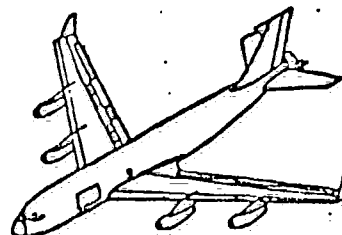
YIELDS 16 VARIABLES / NODE POINT

1005062858

## VERIFICATION TESTS

### CONFIGURATIONS:

- BOUNDED FLOWS
  - TURBULENCE CLOSURE
  - VORTEX STRUCTURES
- FREE JETS
  - ENTRAINMENT
  - DISCRETENESS
  - VORTEX STRUCTURES
- SHEAR LAYERS
  - DECAY RATE
  - REYNOLDS STRESSES



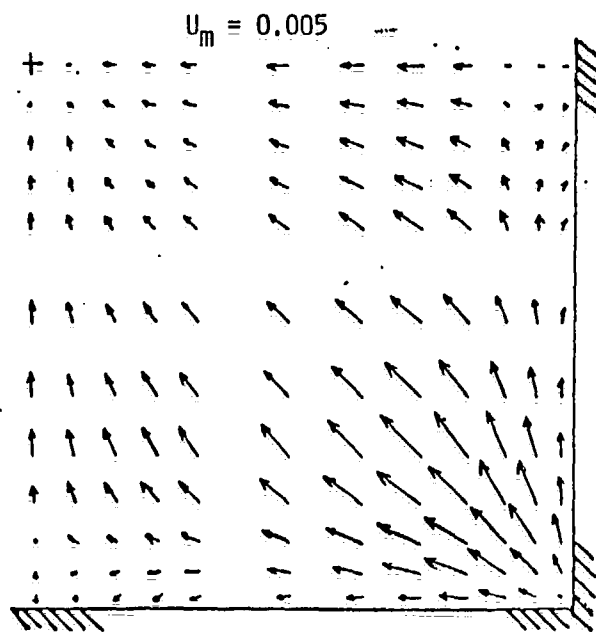
### SOLUTIONS:

- C/M C: 3DPNS COMPUTER PROGRAM
- CDC CYBER / 203

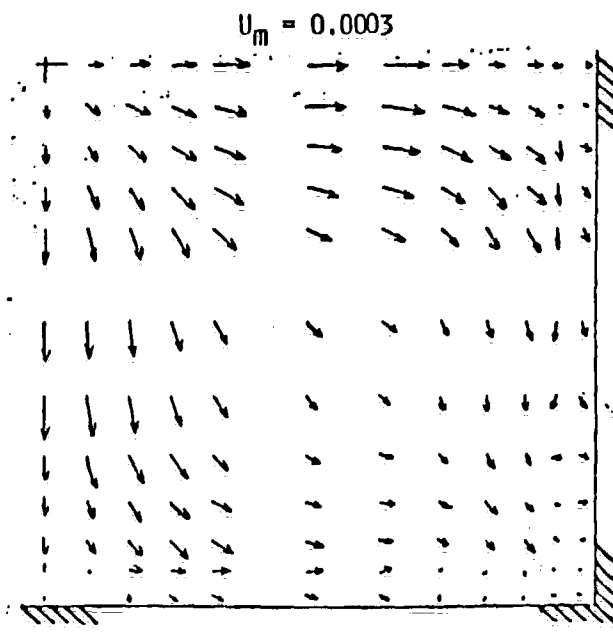
1005062859

3-DIMENSIONAL PARABOLIC NAVIER-STOKES  
TURBULENT FLOW IN RECTANGULAR DUCT  
TRANSVERSE PLANE VELOCITY DISTRIBUTIONS  
(BAKER, ET. AL., ASME, 1981)

MASS CONSERVATION ONLY



EDDY VISCOSITY MODEL,  $x_1/D = 30$ .



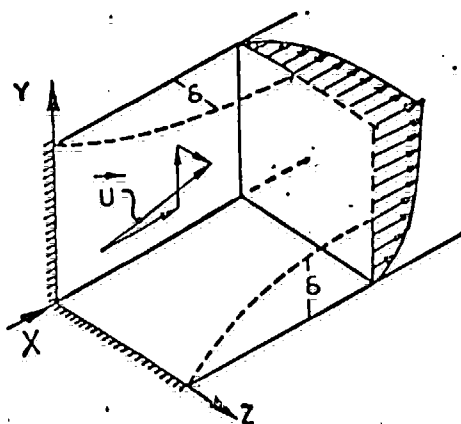
1005062860

# THREE-DIMENSIONAL PARABOLIC NAVIER STOKES

## TURBULENT FLOW IN RECTANGULAR DUCT

### PROBLEM DEFINITIONS

#### BASIC CONFIGURATION



#### BOUNDARY CONDITIONS

$$\begin{aligned} \frac{\partial}{\partial x_n} (\tilde{u}_3, k, \epsilon, p_p, \phi) &\equiv 0 \\ \frac{\partial}{\partial x_n} (\tilde{u}_2, k, \epsilon, p_p, \phi) &\equiv 0 \\ (\tilde{u}_1, \tilde{u}_2, \tilde{u}_3, k, \epsilon, p_p, \phi) &\equiv 0 \end{aligned}$$

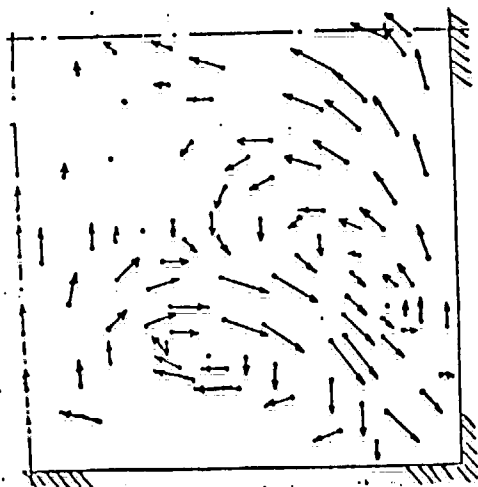
1005062861

3-DIMENSIONAL PARABOLIC NAVIER-STOKES  
TURBULENT FLOW IN RECTANGULAR DUCT  
TRANSVERSE PLANE VELOCITY DISTRIBUTIONS

EXPERIMENTAL DATA,  $X/D = 37$

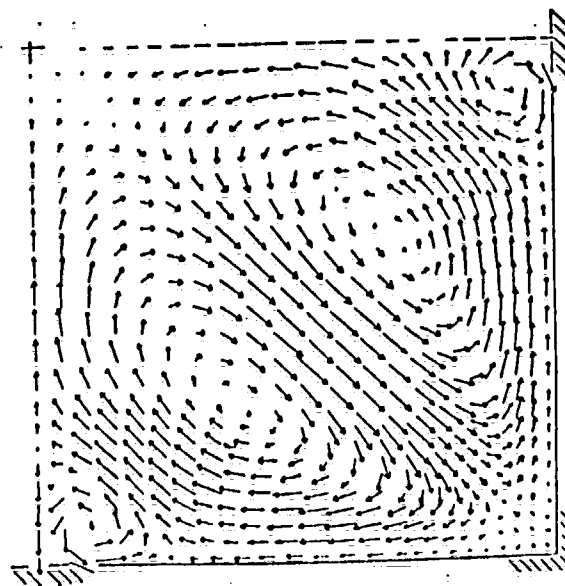
MELLING & WHITELAW (JFM, 1976)

$u^M = .008$



FINER DISCRETIZATION  $M = 25^2$

BAKER et al. (AIAA J, 1983)  $u^M = .004$



1005062862



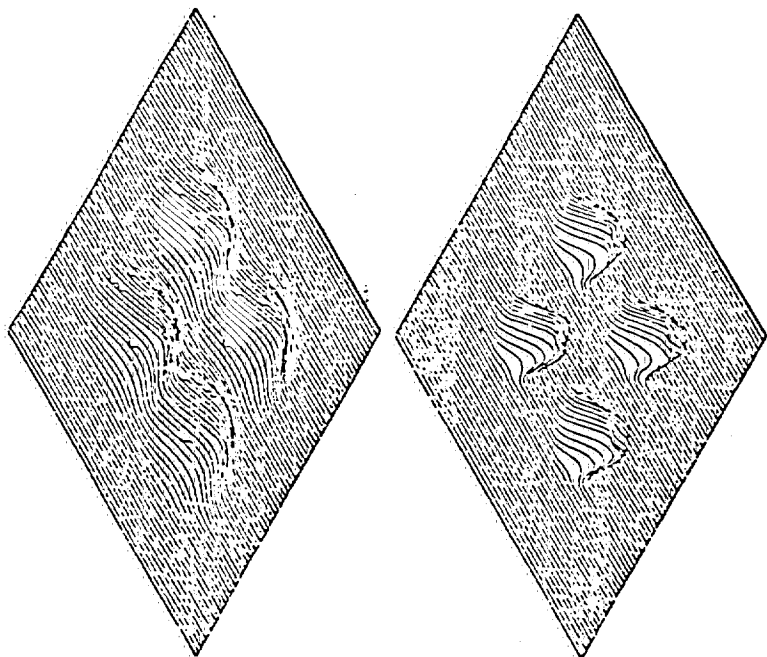


Figure 11. Penalty Algorithm Prediction of Turbulent Kinetic Energy Distributions, Four Multiple Jet Geometry,  $u_j = 12$  m/s, a)  $x_j/R = 0.0$ ,  $k_0 = 0.005$ , b)  $x_j/R = 0.12$ ,  $k_m = 0.02$ , c)  $x_j/R = 0.25$ ,  $k_m = 0.035$ , d)  $x_j/R = 1.5$ ,  $k_m = 0.039$ .

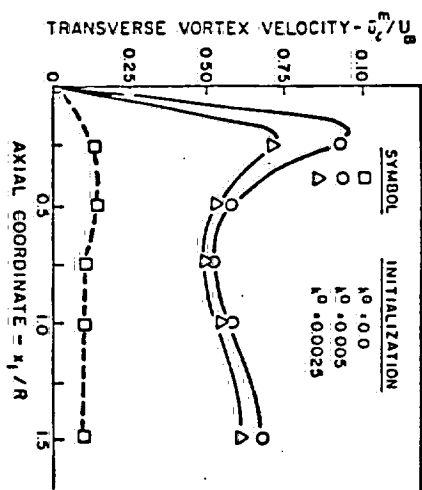
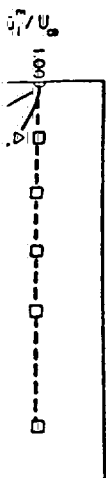
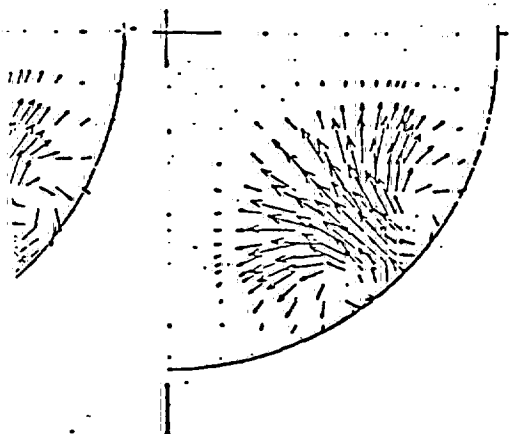


Figure 13. Summary of Penalty Algorithm Prediction of Transverse Plane Mean Velocity  $u_x$  Extrema as Function of Jet Initial Turbulent Kinetic Energy Level.



1005062863

Figure 11. Penalty Algorithm Prediction of Turbulent Kinetic Energy Distributions, Four Multiple Jet Geometry,  $\bar{u}_1 = 12$  m/s, a)  $x_1/R = 0.0$ ,  $k^0 = 0.005$ , b)  $x_1/R = 0.12$ ,  $k_m = 0.02$ , c)  $x_1/R = 0.25$ ,  $k_m = 0.035$ , d)  $x_1/R = 1.5$ ,  $k_m = 0.039$ .

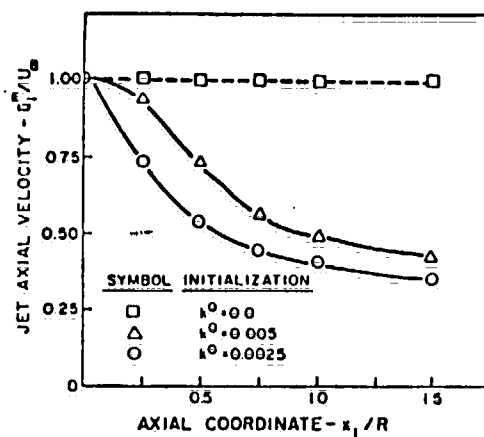
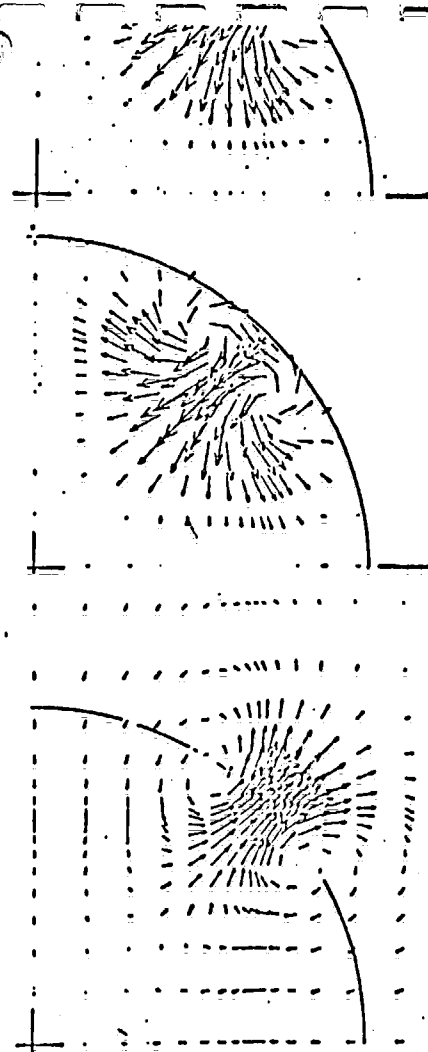


Figure 12. Summary of Penalty Algorithm Prediction of Axial Mean Velocity  $\bar{u}_1$  Decay as Function of Jet Initial Turbulent Kinetic Energy Level.

Figure 14. Penalty Algorithm Prediction of Transverse Plane Mean Velocity  $\bar{u}_1$  Distributions as Function of Locator Radius Extension, Four Multiple Jet Geometry,  $\bar{u}_1 = 12$  m/s, a) One-Millimeter Extension,  $x_1/R = 0.25$ ,  $u_1^0 = 0.182$ , b) Three-Millimeter Extension,  $x_1/R = 0.75$ ,  $u_1^0 = 0.052$ , c) One-Millimeter Extension,  $x_1/R = 1.5$ ,  $u_1^0 = 0.055$ .



1005062864

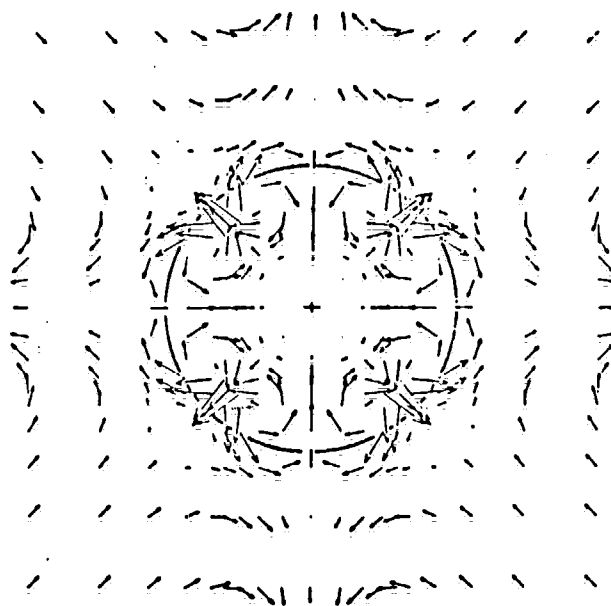


Figure 15. Penalty Algorithm Prediction of Transverse Plane Velocity  $\bar{u}_g$  Distribution On Half Discretization of Full Solution Domain,  $\bar{u}_1^0 = 12$  m/s,  $x_1/R = 1.5$ ,  $u_{11}^0 = 0.084$ ,  $M = 19 \times 19$ .

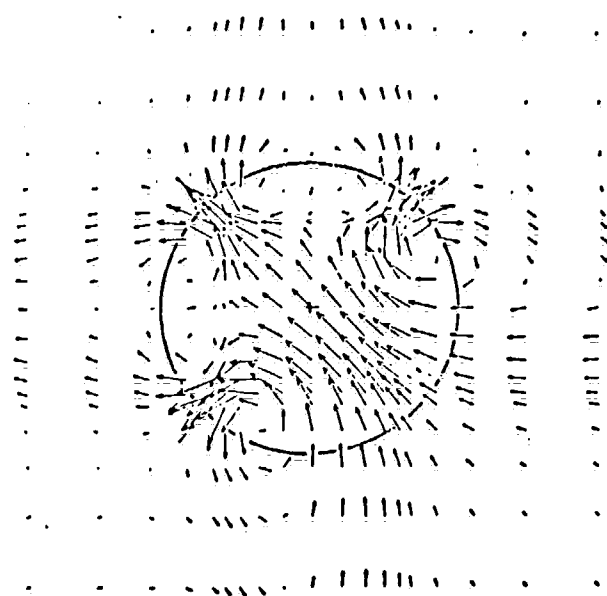
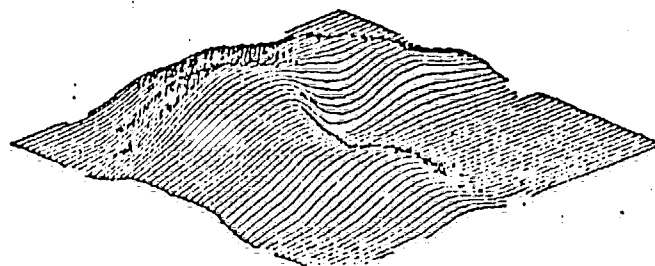
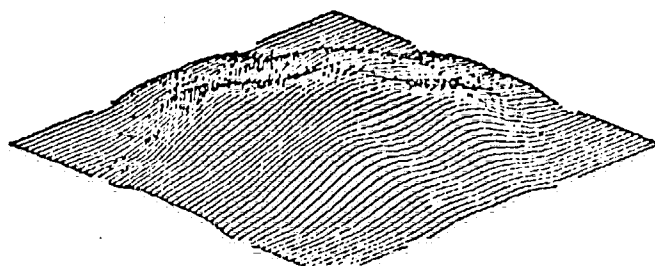


Figure 16. Penalty Algorithm Prediction of Transverse Plane Velocity  $\bar{u}_g$  Distribution, Four Multiple Jet Geometry with One Jet Off,  $\bar{u}_1^0 = 12$  m/s,  $x_1/R = 1.5$ ,  $u_{11}^0 = 0.126$ ,  $M = 19 \times 19$ .



1005062865

0.084,  $M = 19 \times 19$ .

$\frac{u_{11}}{Q} = 0.1$ ,  $III = 14 \times 14$ .

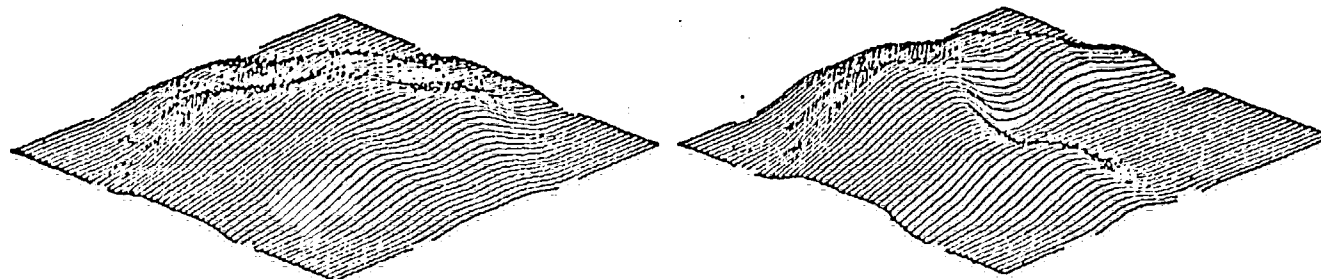
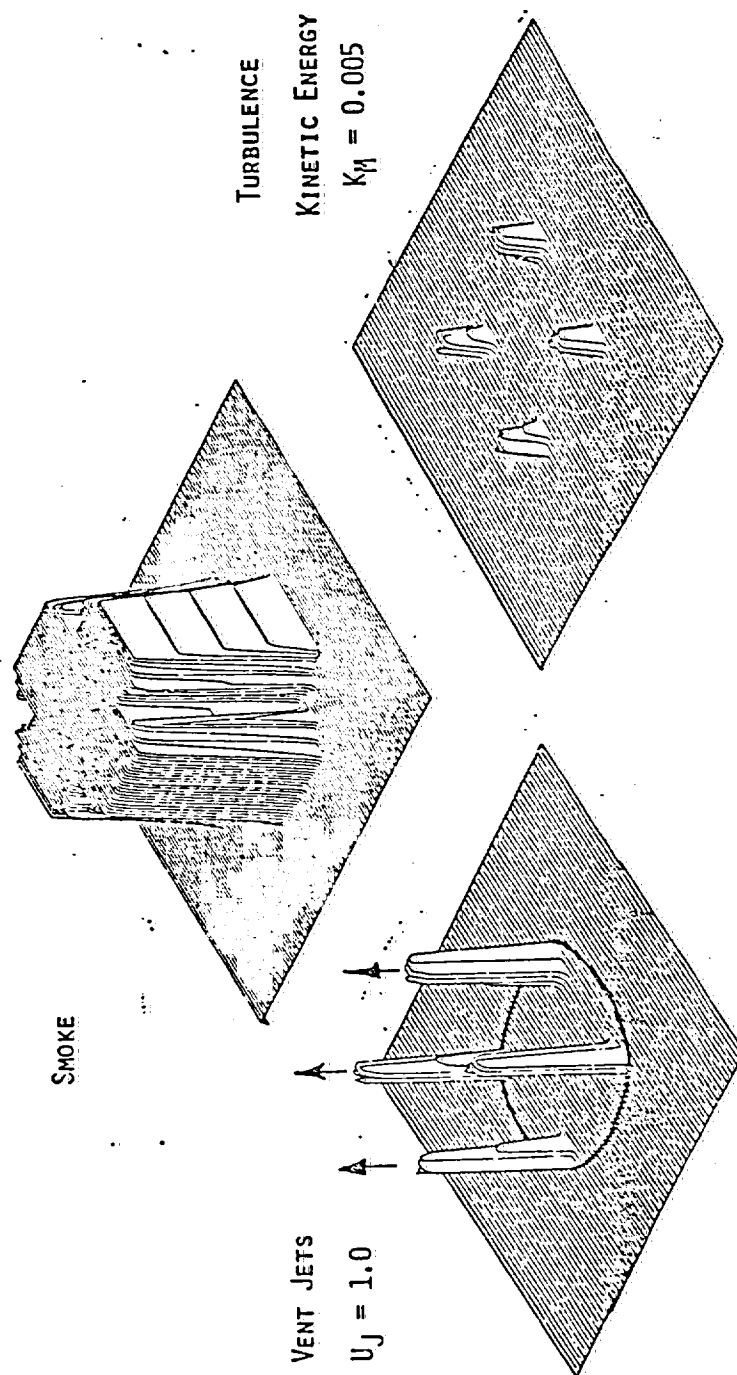


Figure 17. Penalty Algorithm Prediction of Smoke Visualization Distributions On Full Solution Domain,  $\bar{u}_1^0 = 12$  m/s,  $x_1/R = 6.0$ , a) Four Jets Operating,  $Y_m = 53\%$ , b) Three Jets Operating,  $Y_m = 59\%$ .

1005062866

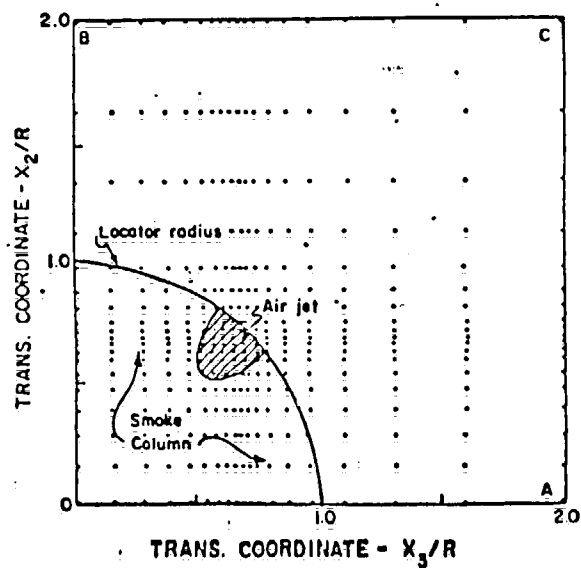
C M C: 3DPNS ANALYSIS - INITIAL CONDITIONS



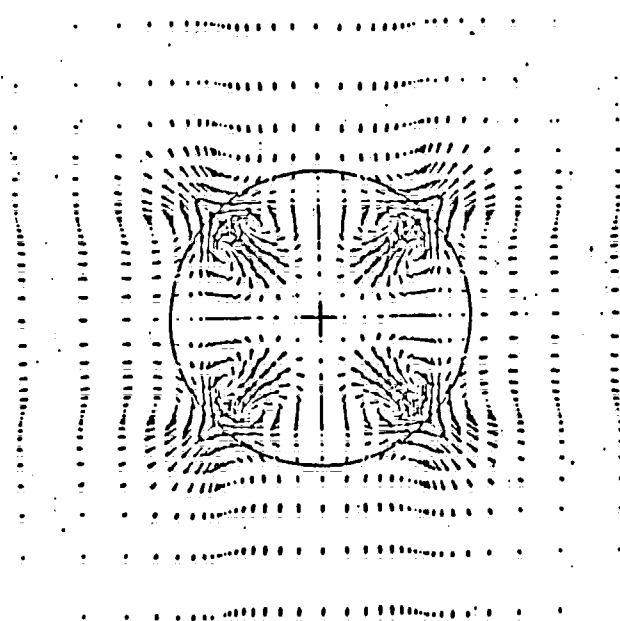
1005062869

THREE-DIMENSIONAL PARABOLIC NAVIER-STOKES  
MULTIPLE FREE-JET SECONDARY VORTEX FIELD  
3DPNS ANALYSIS DESCRIPTION

GEOMETRY / DISCRETIZATION

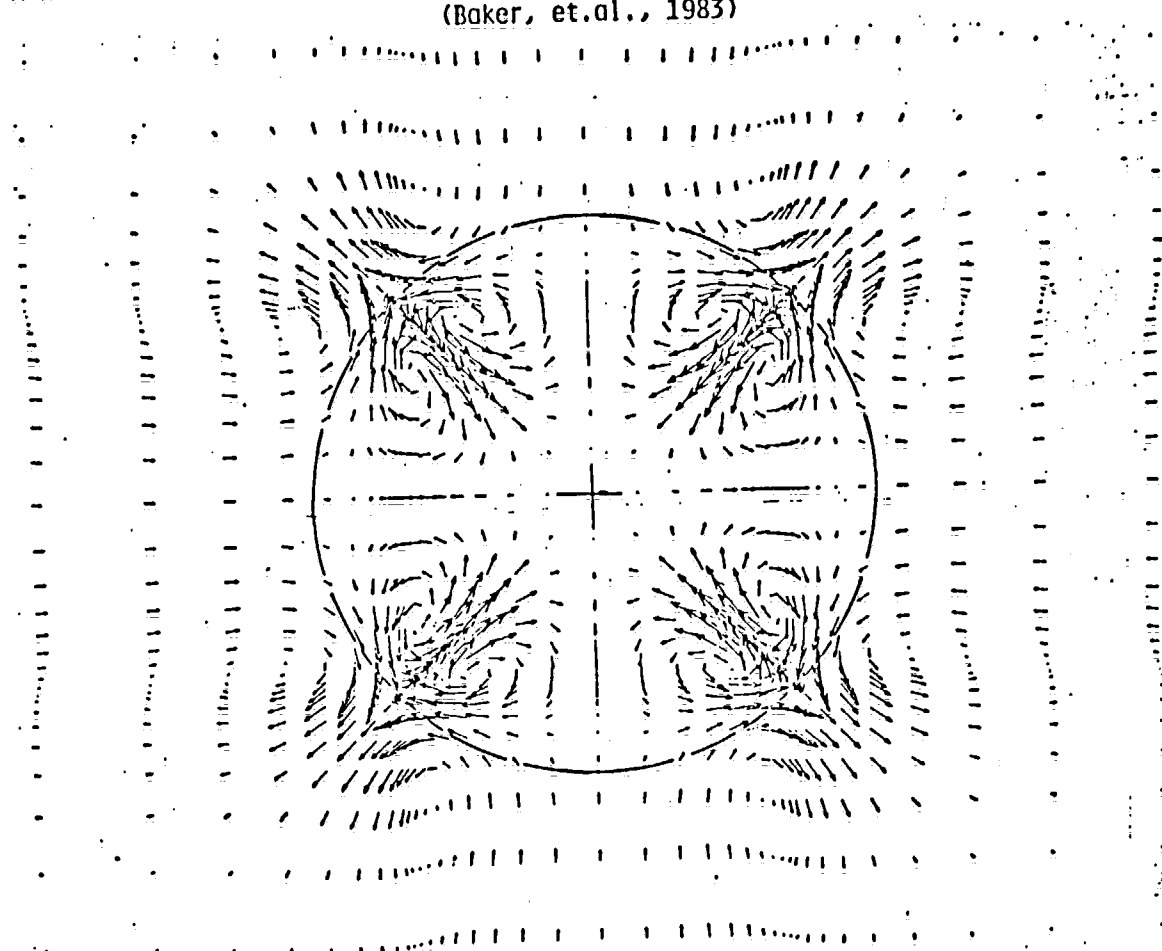


TRANSVERSE PLANE VORTEX FIELD



1005062870

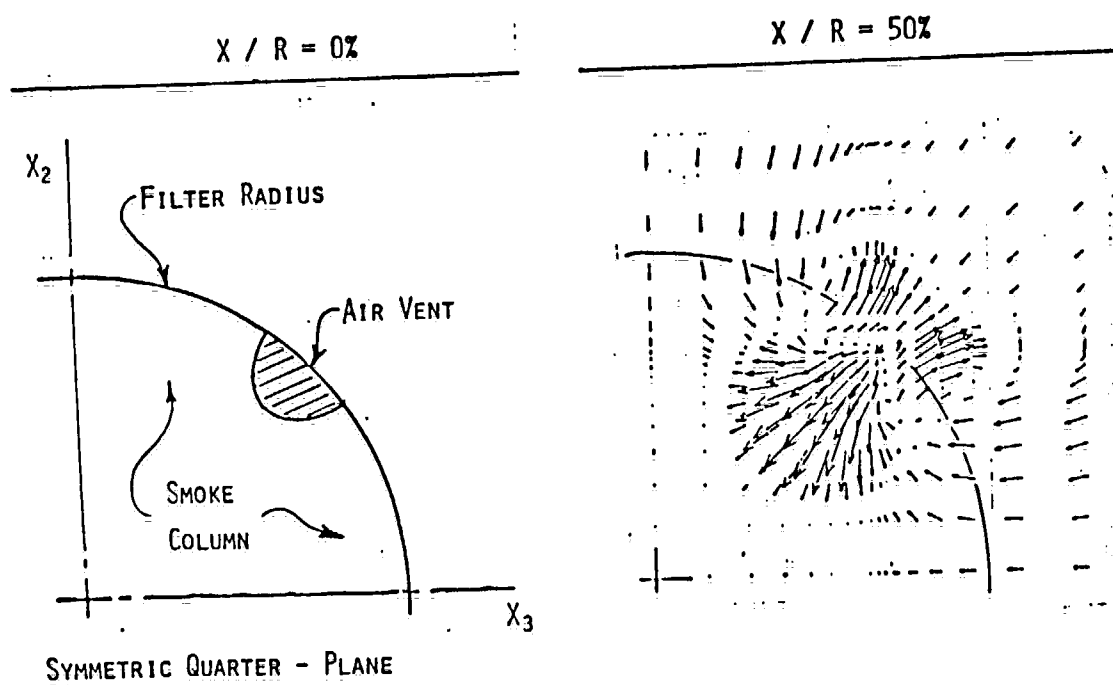
SECONDARY VORTEX FLOW DUE TO FOUR TURBULENT FREE JETS  
(Baker, et.al., 1983)



1005062871

# ACTRON FILTER

## GENERATION OF VORTEX VELOCITY FIELD



1005062872

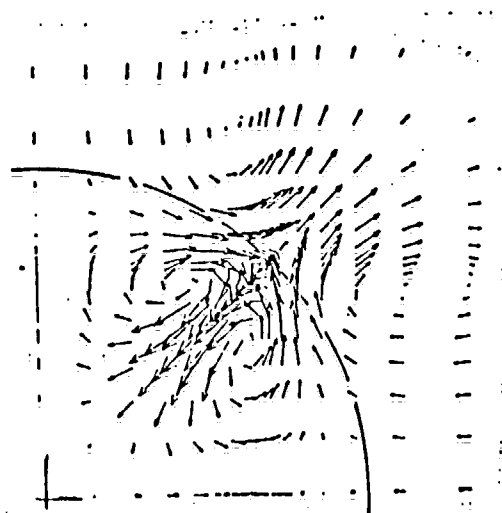


ACTRON FILTER  
GENERATION OF VORTEX VELOCITY FIELD

$X / R = 100\%$



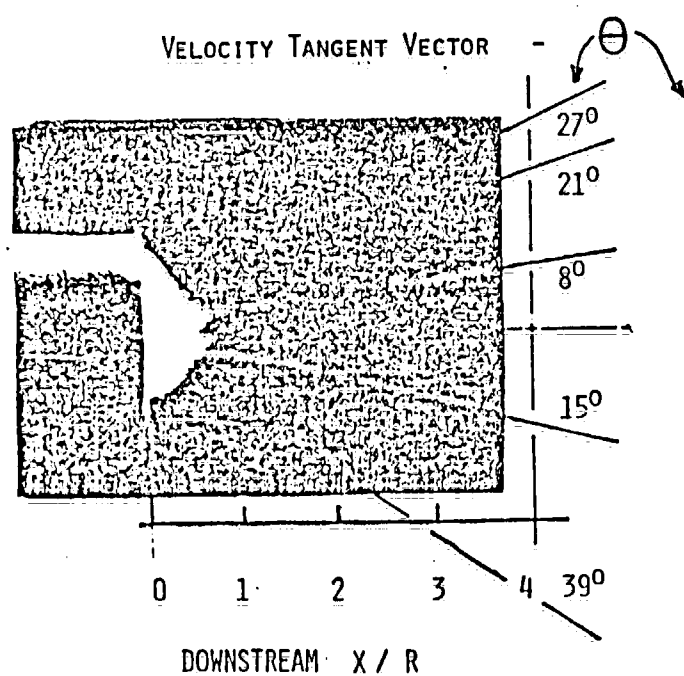
$X / R = 150\%$



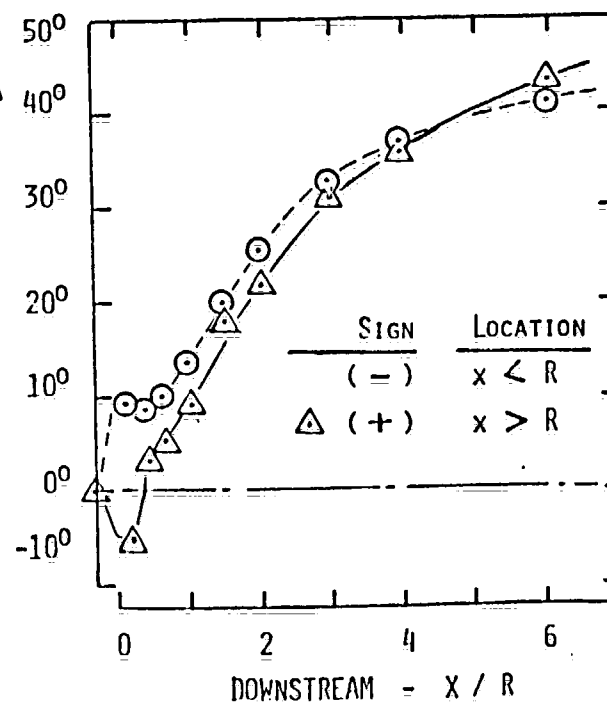
1005062873

THREE-DIMENSIONAL PARABOLIC NAVIER-STOKES  
 MULTIPLE FREE-JET SECONDARY VORTEX FIELD  
 EXTREMUM VORTEX VELOCITY FIELD COMPARISONS

SMOKE FLOW VISUALIZATION

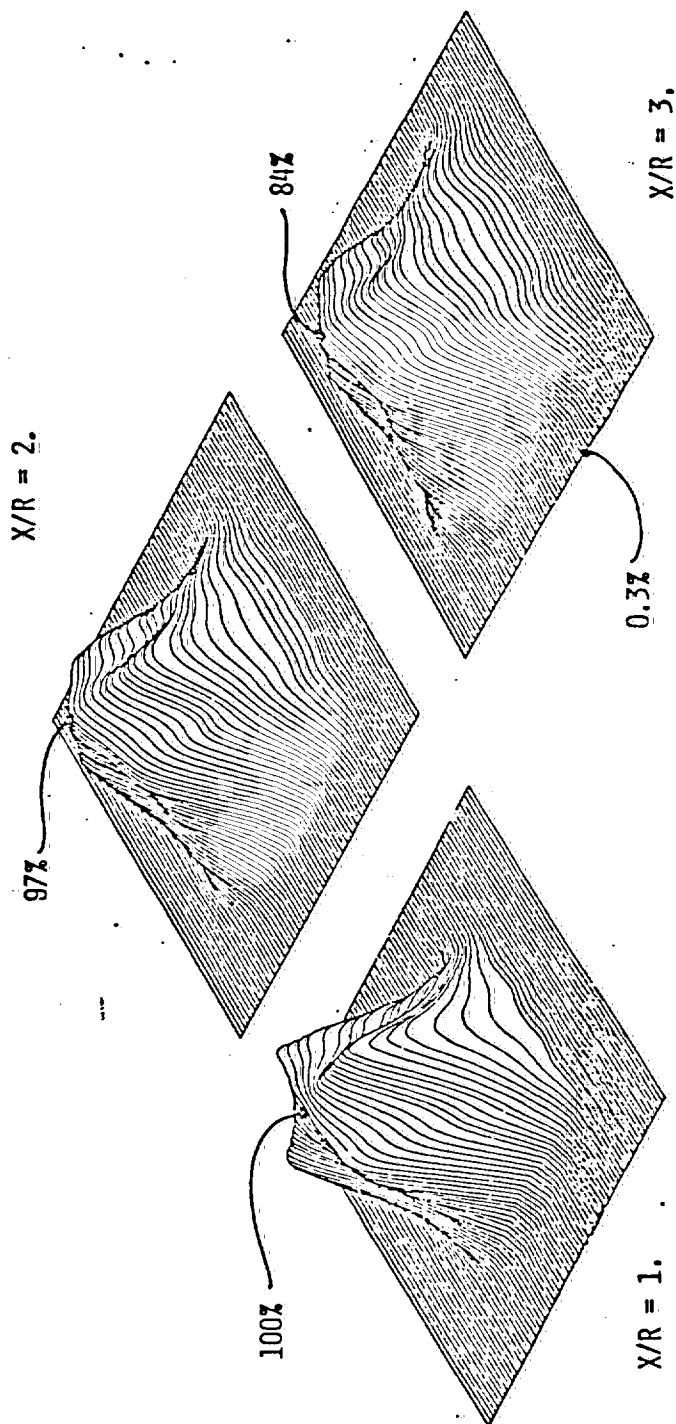


3DPNS PREDICTION



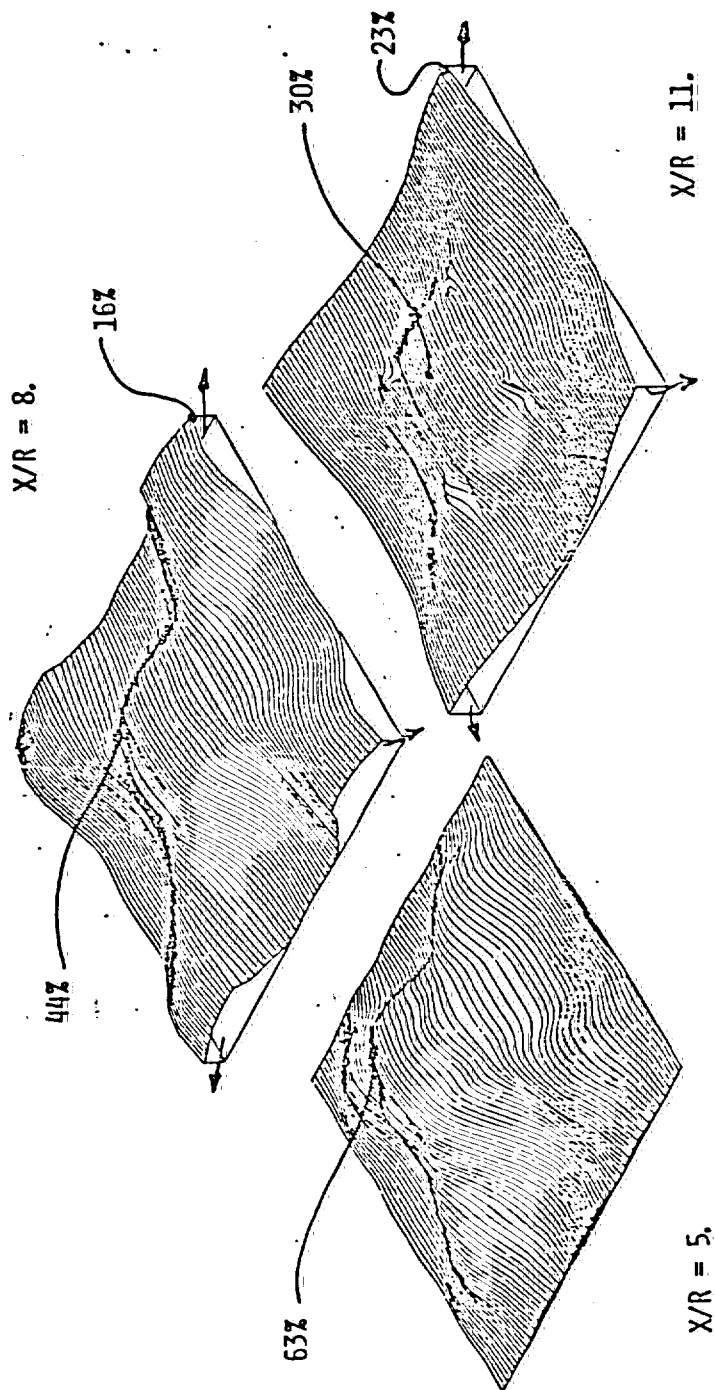
1005062874

C M C: 3DPNS ANALYSIS - DISPERSION OF SMOKE  
STANDARD INITIATION, 7° SWIRL



1005062875

C M C: 3DPNS ANALYSIS - DISPERSION OF SMOKE  
STANDARD INITIATION, 7° SHIRL

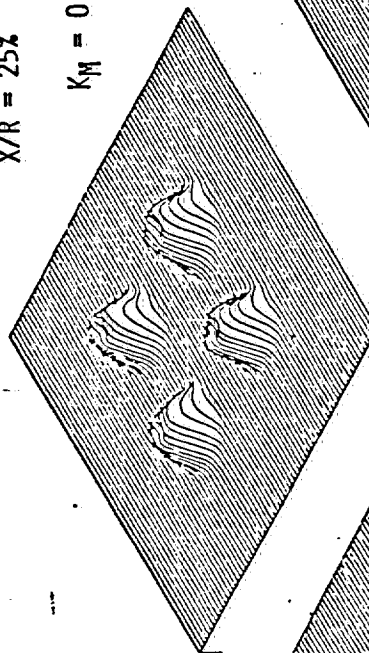


1005062876

C M C: 3DPNS ANALYSIS - TURB. KINETIC ENERGY  
STANDARD INITIATION - NO 7° SWIRL

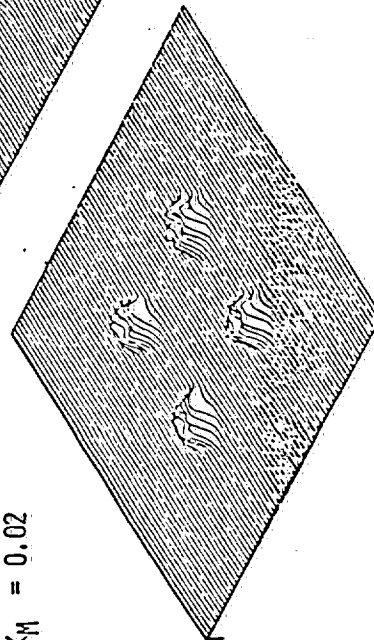
X/R = 25%

$K_M = 0.035$



X/R = 12%

$K_M = 0.02$



X/R = 150%

$K_M = 0.039$



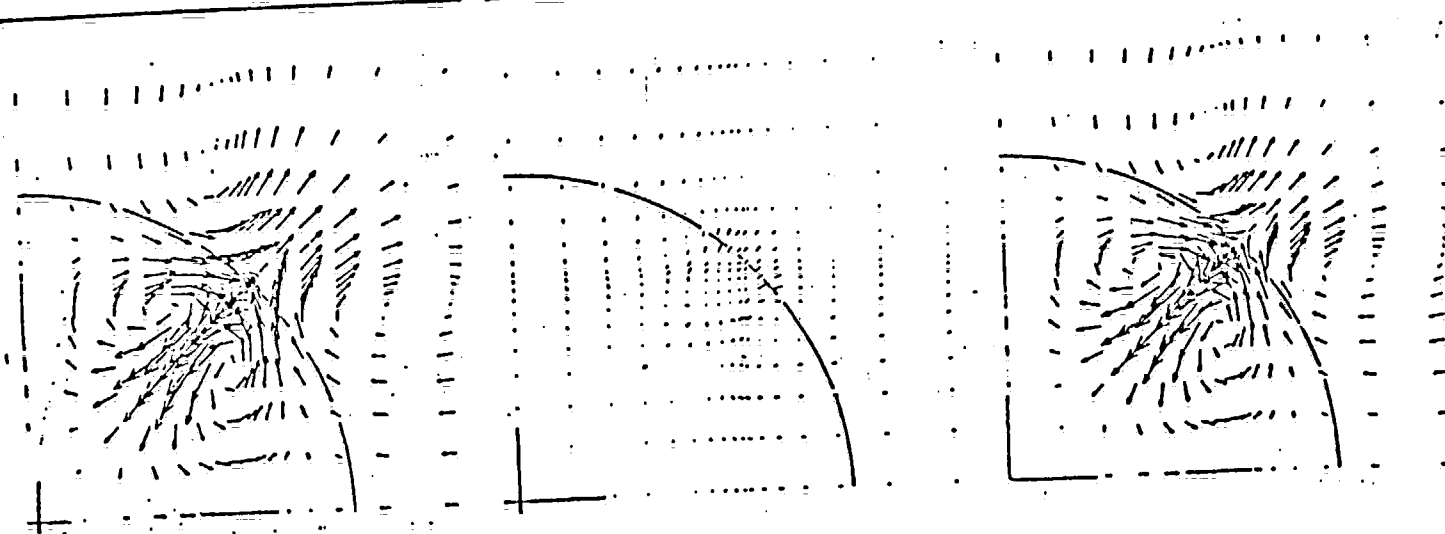
1005062877

THREE-DIMENSIONAL PARABOLIC NAVIER-STOKES  
 MULTIPLE FREE-JET SECONDARY VORTEX FIELD  
 INFLUENCE OF INITIAL TURBULENCE UNCERTAINTY -  $X/R = 1.5$

$$k^0 = 0.005, \quad u_{\ell}^M = 0.067$$

$$k^0 = 0, \quad u_{\ell}^M = 0.009,$$

$$k^0 = 0.0025, \quad u_{\ell}^M = 0.059$$

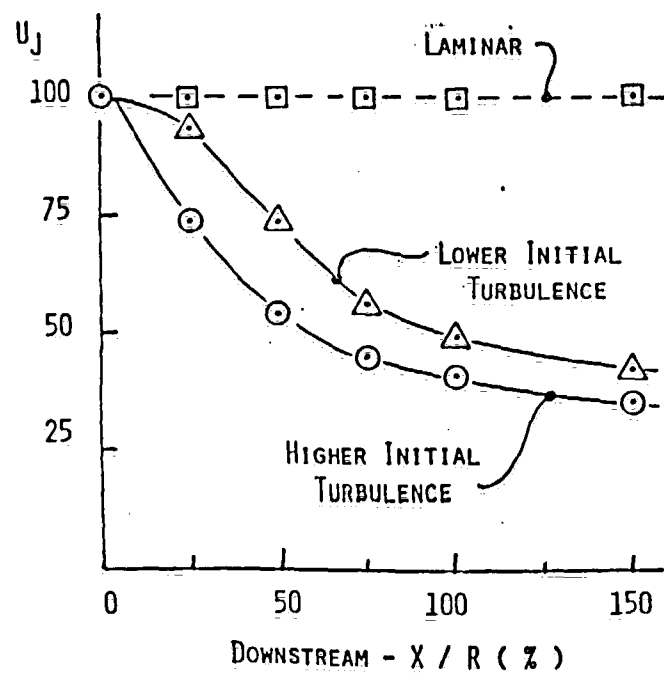


1005062878

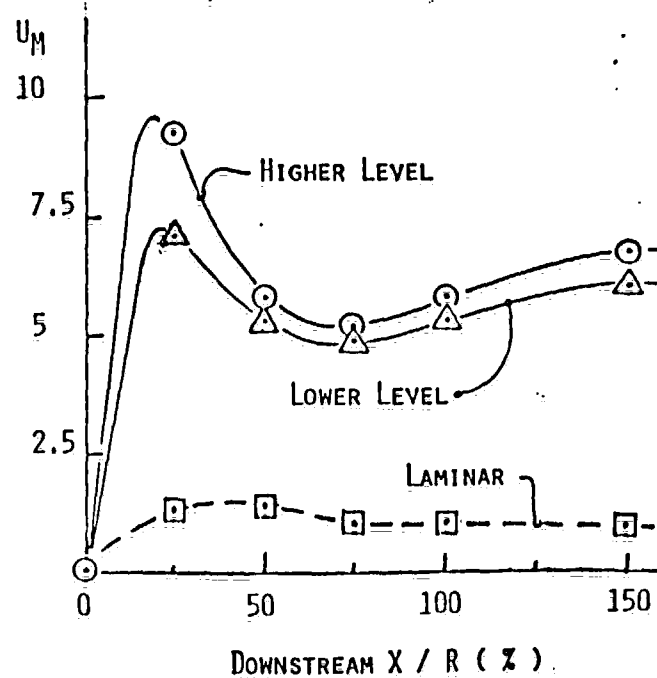
# ACTRON FILTER

## EFFECT OF TURBULENCE ON AERODYNAMICS

VENT VELOCITY DECAY

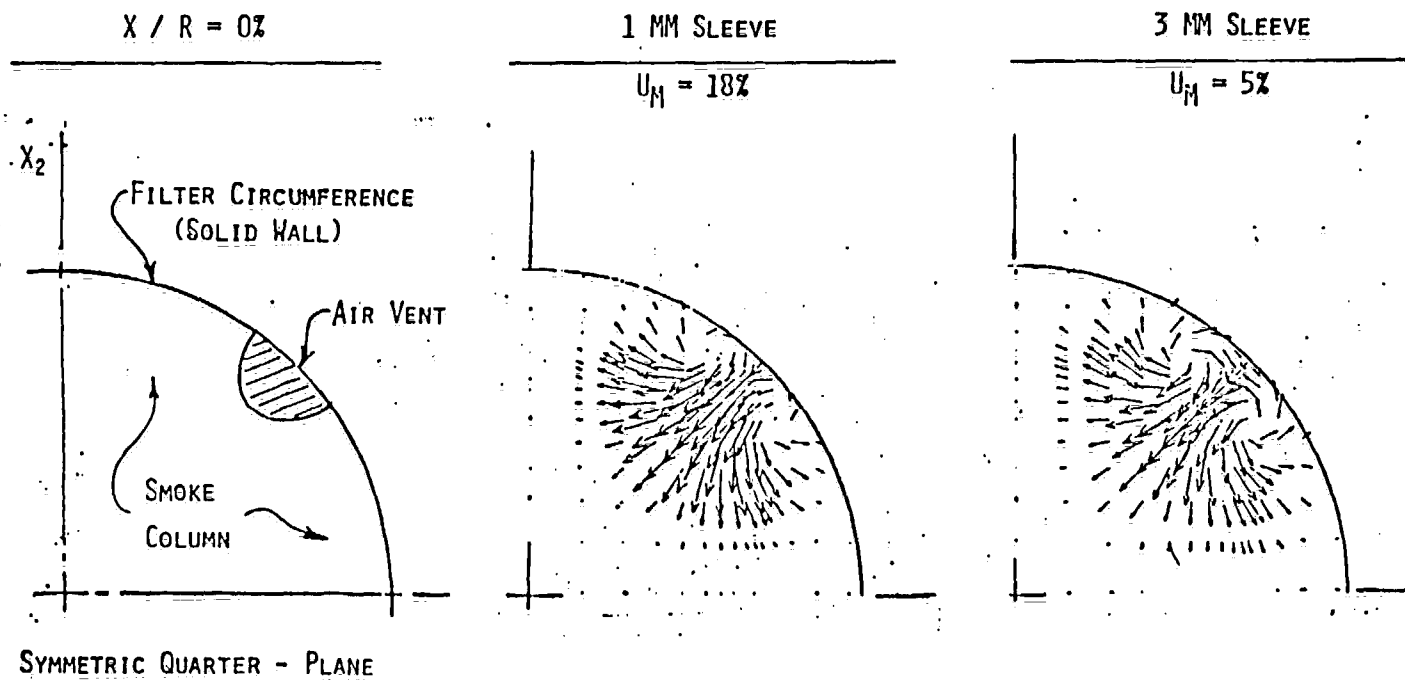


VORTEX VELOCITY MAXIMUM



1005062879

ACTRON FILTER  
SLEEVE EFFECT ON VORTEX VELOCITY FIELD

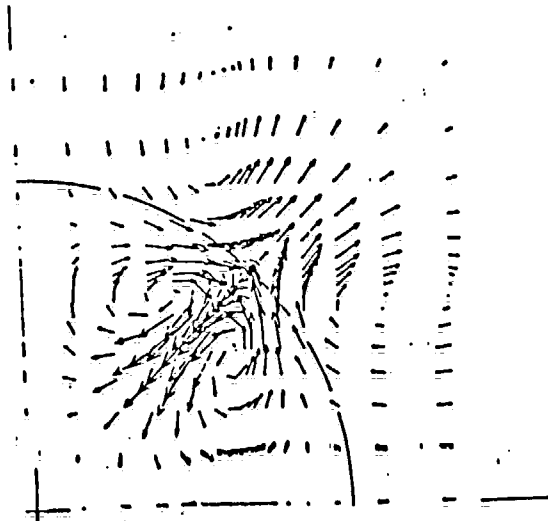


1005062880

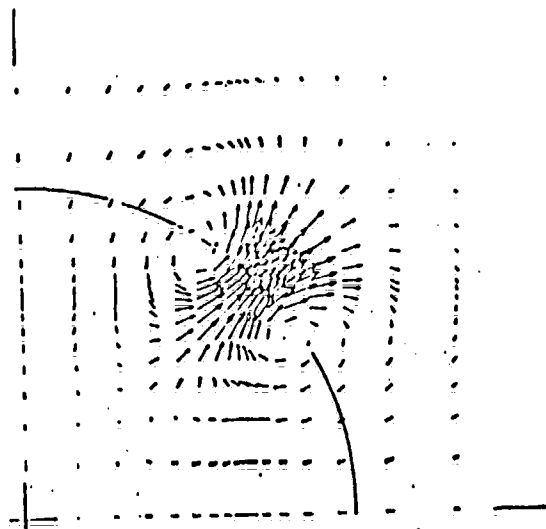


ACTRON FILTER  
VORTEX VELOCITY FIELD,  $X/R = 150\%$

No SLEEVE,  $U_M = 7\%$



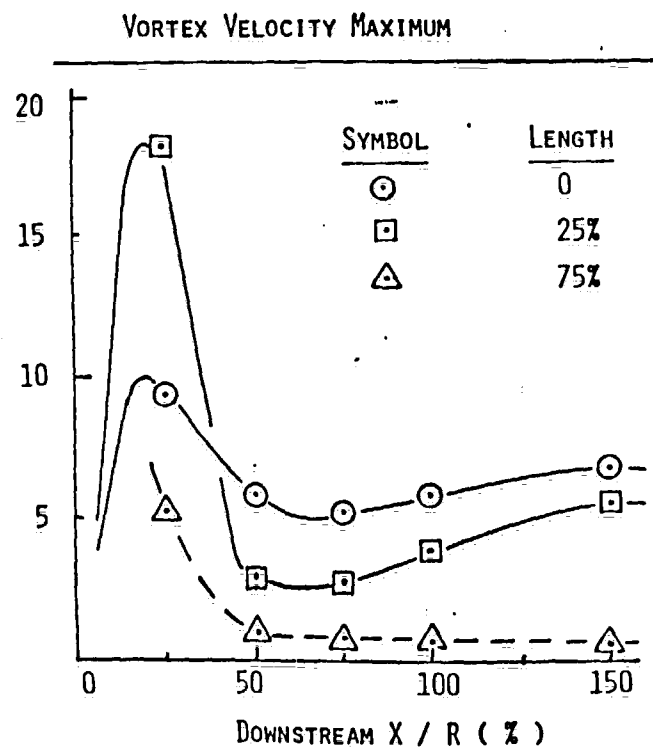
1 MM SLEEVE,  $U_M = 5\%$



1005062881

# ACTRON FILTER

## AERODYNAMICS MODIFICATIONS BY SLEEVED VENT



### ESSENTIAL ACTION

#### NEARFIELD

- ENHANCE VENT DECAY
- PREVENT ENTRAINMENT
- STRENGTHEN VORTEX

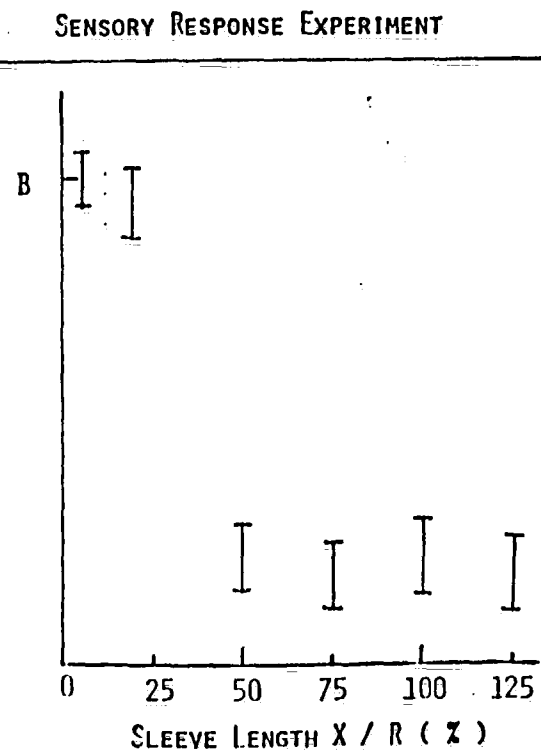
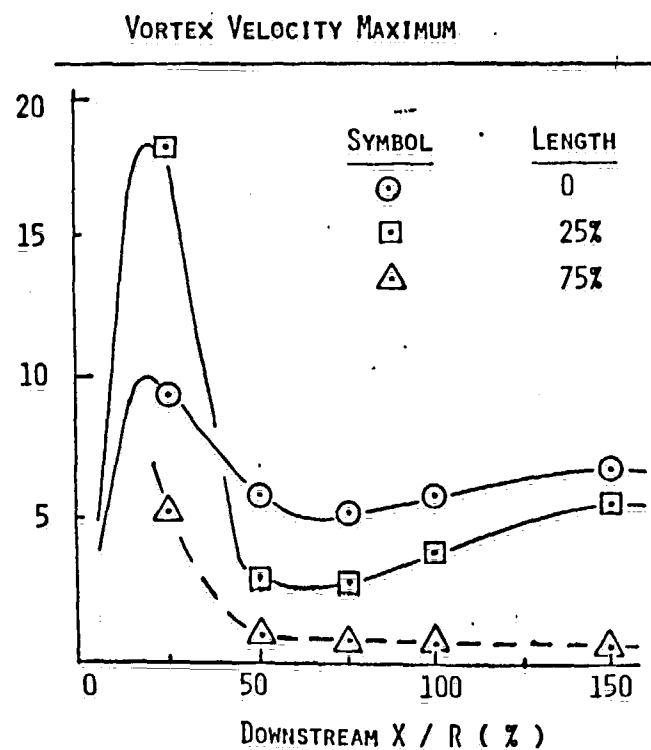
#### FARTHER FIELD

- DISSIPATE VENT
- NO ENTRAINMENT
- WEAKEN VORTEX

1005062882

# ACTRON FILTER

## AERODYNAMICS MODIFICATIONS BY SLEEVED VENT



1005062883

# PREDICTION OF SECONDARY VORTEX FLOWFIELDS INDUCED BY MULTIPLE FREE-JETS ISSUING IN CLOSE PROXIMITY

A. J. Baker\*, J. A. Orzechowski\*\*, and G. E. Stungis\*

## Abstract

A continuity-constraint finite element numerical algorithm, for solution of the three-dimensional parabolic Navier-Stokes equations for subsonic turbulent flows, is applied to prediction of secondary vortex flowfields induced by multiple free-jets issuing in close proximity. The combined action of axial decay of the high speed jets, induced entrainment from the farfield, and geometric discreteness of the jets yields prediction of eight counter-rotating vortex pairs for a four-jet configuration. The extremum magnitude of the induced transverse vortex velocity can exceed 10% of that of the jet initial axial velocity. The results of the numerical predictions compare well with available video-graphic data, including the effects of geometric and initial flowfield modifications.

## I. Introduction

An important aerodynamics problem class is assessment of the steady-flow interaction of multiple subsonic free-jets issued in close proximity. Dependent upon geometric parameters, and whether the jets are laminar or turbulent, this uniaxial initial configuration can induce detailed three-dimensional velocity fields characterized by large scale vortex structures. A substantial challenge in computational fluid mechanics is to identify and evaluate a numerical solution algorithm for prediction of this type of three-dimensional turbulent flowfield.

Figure 1 illustrates the essential geometry of a representative aerodynamic multi-jet system. Provided there is no reversal of the dominant component of velocity, parallel to the axis of the jets, the three-dimensional parabolic Navier-Stokes (PNS) equation system is a candidate for solution of the problem class. A formal order of magnitude PNS analysis confirms that axial diffusion processes are negligible, and that the transverse momentum equations govern transverse plane pressure distributions. The continuity equation governs first order effects on momentum. For the free-jet problem class, the complementary solution to the resultant pressure Poisson equation is a homogeneous constant, where the Poisson equation is obtained from the divergence of the transverse momentum equations. A turbulence closure model is also required, and the parabolic form of the two-equation turbulence kinetic energy-isotropic dissipation system is representative of the minimum acceptable level of simplicity.

With the basic governing equation system thus defined, construction of a suitable algorithm requires addressing the ordering analysis and the farfield

boundary conditions. A primitive variables formulation must rearrange the continuity equation to yield a deterministic system for transverse velocities, cf. Baker et al.<sup>1</sup>, Dodge<sup>2</sup>, Patankar<sup>3</sup>. Alternatively, a vector potential function can be defined to identically satisfy the continuity equation, and a vorticity equation derived to replace the transverse momentum equations, cf. Briley et al.<sup>4</sup>, Ghia et al.<sup>5</sup>. One dominant factor controlling this basic decision is that the multiple free-jet solution domain is unbounded. Hence, flowfield specification in the farfield is a priori unknown, i.e., the entrainment action of the jet interaction that induces inflow/efflux across surfaces located arbitrary distances from the jet is a solution output. For this required flexibility, and the inherent mathematical robustness, the finite element penalty function algorithm<sup>1</sup> was selected. This paper presents a statement of the algorithm, boundary condition specifications, and the results of computational experiments compared with experimental data.

## II. Problem Statement

The three-dimensional PNS equation system for the steady, subsonic turbulent flow of an isoenergetic fluid, to the principal scale of ordering<sup>1</sup>, is

$$L(\bar{p}) = \frac{\partial}{\partial x_j} [\bar{p} u_j] = 0 \quad (1)$$

$$L(\bar{u}_1) = \frac{\partial}{\partial x_1} [\bar{p} u_1 \bar{u}_1 + \bar{p}] + \frac{\partial}{\partial x_2} [\bar{p} u_1 \bar{u}_2 + \bar{p} u_1 u_2] - \frac{1}{Re} \frac{\partial \bar{u}_1}{\partial x_1} = 0 \quad (2)$$

$$L(\bar{u}_k) = \frac{\partial \bar{p}}{\partial x_k} + \frac{\partial}{\partial x_1} [\bar{p} u_k \bar{u}_1] = 0 \quad (3)$$

$$L(k) = \frac{\partial}{\partial x_1} [\bar{p} u_1 k] + \frac{\partial}{\partial x_2} [\bar{p} u_2 k + \bar{p} C_k \frac{k}{\epsilon} \bar{u}_2 u_2] - \bar{u}_2 \frac{\partial k}{\partial x_1} + \bar{p} u_1 u_2 \frac{\partial \bar{u}_1}{\partial x_1} + \bar{p} \epsilon = 0 \quad (4)$$

$$L(\epsilon) = \frac{\partial}{\partial x_1} [\bar{p} u_1 \epsilon] + \frac{\partial}{\partial x_2} [\bar{p} u_2 \epsilon + \bar{p} C_\epsilon \frac{k}{\epsilon} \bar{u}_2 u_2 \frac{\partial \epsilon}{\partial x_1}] + C_\epsilon^2 \bar{p} \frac{\epsilon}{u_1 u_2 k} \frac{\partial \bar{u}_1}{\partial x_1} + C_\epsilon^2 \bar{p} \frac{\epsilon^2}{k} = 0 \quad (5)$$

The variables appearing in equations 1-5 have their usual interpretation in fluid mechanics, where superscript bar denotes conventional time averaging<sup>6</sup>, and the cross coupling of fluctuations in density and velocity have been assumed negligible. The tensor index summation convention is implied, with  $x_j$  aligned with the principal flow direction, and  $1 \leq j \leq 3$  and  $2 \leq (k,l) \leq 3$ . The turbulence kinetic energy  $k$  is the trace of the Reynolds stress tensor,  $\epsilon$  is the isotropic dissipation function, and  $Re$  is the characteristic Reynolds number.

\*Professor of Engineering Science, University of Tennessee, Knoxville, TN, Associate Fellow AIAA.

\*\*Principal Programmer, Computational Mechanics Consultants, Inc., Knoxville, TN.

\*Research Consultant, Brown & Williamson Tobacco Corp., Louisville, KY.

1005062884

For the reported results, the Reynolds stress tensor field constitutive model of Baker et al.<sup>1</sup> is employed. The PNS ordering analysis indicates the extremum significance of components of  $u_i u_j$  is one order smaller than unity. Simplifying the constitutive equation to this order yields

$$\begin{aligned}\overline{u_1 u_1} &= C_1 k - C_2 C_4 \frac{k^3}{c^2} \left[ \left( \frac{\partial u_1}{\partial x_2} \right)^2 + \left( \frac{\partial u_2}{\partial x_1} \right)^2 \right] \\ \overline{u_2 u_2} &= C_1 k - C_2 C_4 \frac{k^3}{c^2} \left( \frac{\partial u_1}{\partial x_2} \right)^2 \\ \overline{u_1 u_2} &= C_1 k - C_2 C_4 \frac{k^3}{c^2} \left( \frac{\partial u_1}{\partial x_2} \right)^2 \\ \overline{u_1 u_3} &= -C_4 \frac{k^2}{c} \frac{\partial u_1}{\partial x_2} \\ \overline{u_2 u_3} &= -C_4 \frac{k^2}{c} \frac{\partial u_1}{\partial x_2} \\ \overline{u_3 u_3} &= -C_2 C_4 \frac{k^3}{c^2} \left[ \frac{\partial u_1}{\partial x_2} \frac{\partial u_1}{\partial x_2} \right]\end{aligned}\quad (6)$$

The coefficients  $C_\alpha$ ,  $1 \leq \alpha \leq 4$ , in equation 6 are correlation constants; the standard values  $C_\alpha = \{0.94, 0.067, 0.56, 0.068\}$  were used for the present study.

In the primitive form, equations 1-6 do not represent a well-posed initial-boundary value problem description for the subsonic flow, multiple free-jet problem class. As a consequence of the ordering, the scalar continuity equation governs both components of velocity in the transverse plane perpendicular to  $x_1$ . As cited in the Introduction, various algorithm constructions have been formulated to address this issue. The approach taken in the present analysis is to employ a finite element penalty function formulation, and to append the order (6) transverse plane momentum equations,

$$L^6(\bar{u}_k) = \frac{\partial}{\partial x_1} \left[ \bar{u}_1 \bar{u}_k \right] + \frac{\partial}{\partial x_2} \left[ \bar{u}_2 \bar{u}_k - \frac{1}{Re} \frac{\partial \bar{u}_k}{\partial x_2} \right] = 0 \quad (7)$$

to equation 3. Further, equation 3 is rearranged to the pressure Poisson equation.

$$L(\bar{p}) \equiv \frac{\partial}{\partial x_k} L(\bar{u}_k) = \frac{\partial}{\partial x_k} \left[ \frac{\partial \bar{p}}{\partial x_k} \right] + \frac{\partial}{\partial x_1} \left( \bar{p} \frac{\partial \bar{u}_k}{\partial x_1} \right) = 0 \quad (8)$$

Equation 8 represents a quasi-linear elliptic boundary value problem, possessing complementary and particular solutions<sup>1</sup>. For the free-jet problem class, the complementary solution is a homogeneous constant equal to the farfield reference pressure. The particular solution to equation 8 is thus obtained using homogeneous Dirichlet boundary conditions. Upon addition of equations 3 and 7,  $L(\bar{u}_k) = L^6(\bar{u}_k)$  represents a well-posed initial-boundary value problem for  $\bar{u}_k$ , upon addition of the order (6) terms to the appropriate scalar components of the Reynolds stress tensor, which are

$$\overline{u_1 u_k} \Big|_{\delta^+} = -C_4 \frac{k^2}{c} \left[ \frac{\partial \bar{u}_k}{\partial x_2} + \frac{\partial \bar{u}_k}{\partial x_2} \right] \quad (9)$$

### III. Finite Element Penalty Algorithm

#### Theoretical Statement

For the dependent variable set  $\bar{q}(x_j) = \{\bar{u}_i, k, c, \bar{p}, u_i u_j\}$ , equations 2, 3 + 7, 4, 5, 8, 6 + 9 represent a well-posed, initial-boundary value problem description on the three dimensional domain  $\Omega = R^2 \times x_1 = \{x_1, x_2 \in R^2 \text{ and } x_1 \in [x_1, x_1]\}$ . There is the additional fundamental requirement that equation 1 be rigorously satisfied, since it governs first order phenomena. The problem statement is completed with a polytropic equation of state for determination of  $\bar{p}$  for the isoelectric flow.

As the consequence of the PNS reformulation, each of the first six members of the set  $\bar{q}$  are eligible for constraint, on the boundary  $\partial R$  of  $R^2$ , by a linear combination of Dirichlet and Neumann boundary conditions. The first five of these members are also required specified as an initial-condition on the plane  $R^2 \times x_1$ . No boundary conditions are appropriate for the algebraic equations governing  $\bar{u}_i u_j$ .

The finite element penalty algorithm, for determination of the semi-discrete approximation  $\bar{q}^h(x_j)$  to  $\bar{q}(x_j)$ , is based on classical concepts for differential constraints in the statement of variational boundary value problems. These concepts are extended to the very non-linear PNS problem class using a Galerkin weighted-residuals formulation. Deferring details<sup>7</sup>, the transverse plane domain  $R^2$  is discretized into the union of non-overlapping subdomains  $R_e^2$ , wherein the functional form for the  $x_1$  dependence of the semi-discrete approximation  $\bar{q}^h$  is assumed a priori specifiable. A convenient form is the cardinal basis  $\{N_k(x_1)\}$ , the members of which are polynomials on  $x_1$  complete to degree  $k$ . Hence, the semi-discrete approximation becomes the union of elemental approximations,

$$\bar{q}(x_j) = \bar{q}^h(x_j) \equiv \bigcup_e \bar{q}^e(x_j) \quad (10)$$

$$\bar{q}^e(x_j) \equiv \{N_k(x_1)\}^T \{Q_l(x_1)\}_e \quad (11)$$

where subscript and/or subscript  $e$  denotes pertaining to the (finite element) domain  $R_e^2$ . Further,  $\{Q_l\}_e$  represents the values taken by  $\bar{q}^e$  at the nodes of the domain  $R_e^2$ , and  $1 \leq l \leq 12$  is a tensor index denoting the appropriate (nodal) vector dependent variable set of  $\bar{q}^h$ .

With definition of  $\bar{q}^h$ , equations 10-11 permit direct evaluation of the semi-discrete approximation error  $L(\bar{q}^h)$  in each of the PNS governing differential equations. The basic concept in the calculus of a discretized variational boundary value problem is to render this error extremum in some norm. In the Galerkin weighted-residuals extension of this concept, this is accomplished by requiring this error to be orthogonal to the space of functions  $\{N_k\}$  selected to define the semi-discrete approximation, i.e.,

$$\int_{R^2} \{N_k\} L(\bar{q}^h) dx = \sum_e \int_{R_e^2} \{N_k\} L(\bar{q}^e) dx \equiv 0 \quad (12)$$

1005062885

The middle expression in equation 12 emphasizes that the actual calculus operations are performed on the elemental domains  $R_k$ . The resultant element (column) matrices are projected to the matrix structure of the global domain using the assembly operator  $S_e$ , which is simply matrix addition by rows.

Equation 12 defines the numerical solution algorithm for the complete set  $\bar{q}^h$  with the exception of the combined equations 3 and 7 for  $\bar{u}_k$ . Here, the definition of the extremum must be augmented (penalized) such that the continuity equation is also satisfied. The functional form for this statement, which is an extension of the classical concept<sup>7</sup>, is

$$\int_{R_k} (N_k) \left[ L(\bar{u}_k^h) + L(\bar{p}_k^h) \right] d\tau - \lambda \int_{R_k} \frac{\partial(N_k)}{\partial x_k} L(\bar{p}_k^h) d\tau \approx \{0\} \quad (13)$$

The actual calculus operations defined in equation 13 are again performed on an elemental basis and assembled, and  $\lambda$  is an (arbitrary) parameter penalizing the statement of semi-discrete error orthogonalization for  $\bar{u}_k$ .

Equations 12-13 define the finite element penalty algorithm for the PNS equation system. The theoretical arbitrariness remaining is solely the degree  $k$  of the cardinal basis  $(N_k)$ , spanning either three-sided or four-sided element domains  $R_k$ , and the penalty parameter  $\lambda$  and functional form for  $L(\bar{p}_k^h)$ . However, equations 12-13 are definitions of non-linear matrices, and resolution of the resultant problem definitions in linear algebra remains. For the semi-discrete approximations  $\{\bar{u}_k^h, \bar{p}_k^h\}$ , equations 12-13 are matrix statements expressing the  $x_j$ -ordinary derivative of the appropriate elements of  $\{Q1\}_e$ , equation 11. A Taylor series defines the matrix algebra statement for the assembly of these elements of  $\{Q1\}$ ,  $1 \leq i \leq 5$ , as:

$$\{F1\} \equiv \{Q1\}_{j+1} - \{Q1\}_j - \Delta x \{Q1\}'_{j+0} - \dots \approx \{0\} \quad (14)$$

In equation 14,  $\{Q1\}'_{j+1}$  represents this ordinary derivative evaluated at some location on the interval  $x_{j+1} - x_j = \Delta x$  as defined by the parameter  $0 \leq \theta \leq 1$ .

Equation 12, evaluated for  $\bar{p}^h$  and  $\bar{u}_k^h$ , yields directly the appropriate column matrix statement  $\{F1\} = \{0\}$ ,  $6 \leq i \leq 12$ . Combined with equation 14, the resultant linear algebra statement of the finite element penalty algorithm for the PNS equation system, becomes

$$\{F1(k, \lambda, \theta, \Delta x, \{Q1\})\} = \{0\} \quad (15)$$

Equation 15 is a highly non-linear algebraic equation system, the character of which is largely determined by the choice of the arbitrary solution parameters  $k$ ,  $\lambda$ ,  $\theta$ , and  $\Delta x$ . Equation 15 does not readily admit a useful linearization, even for  $\theta = 0$  which corresponds to explicit integration. Hence, the appropriate solution statement is the (Newton) matrix solution form,

$$\left[ J(\{F1\}) \right]_{j+1}^p \{Q1\}_{j+1}^{p+1} = - \{F1\}_{j+1}^p \quad (16)$$

where  $p$  is the iteration index at step  $x_{j+1}$ , and

$$\{Q1\}_{j+1}^{p+1} \equiv \{Q1\}_{j+1}^p + \{Q1\}_{j+1}^{p+1} \quad (17)$$

$$\left[ J(\{F1\}) \right] \equiv \frac{\partial \{F1\}}{\partial \{Q1\}} \quad (18)$$

Equation 17 defines the fully-discrete approximation to the dependent variable set at the nodes of  $UR^2$ , hence also  $q^h(x_j)$  throughout  $R^2$ , see equation 10. Equation 18 defines the (Newton) Jacobian of the non-linear algebraic equation system, equation 15.

#### Some Basic Decisions

Equation 15 delineates the basic decisions to be made regarding implementation of the penalty algorithm into a computer code. In addition, for  $\theta > 0$ , a decision is required regarding approximate construction of the Newton algorithm Jacobian  $[J]$ , equation 18, since its size for the twelve dependent-variable PNS statement is unwieldy on present computers. The decision on  $k$ , equation 11, of course impacts considerably on the "size" of  $[J]$ .

The multiple free jet analyses reported herein were conducted using the CMC:3DPNS computer program. 3-13 Each of the basic decisions have been made and evaluated for this code. The discretization of  $R^2$  is defined as the union of triangular cross-section finite elements spanned by the linear ( $k=1$ ) natural coordinate cardinal basis. The trapezoidal rule is employed for the integration algorithm,  $\theta = 1/2$  in equation 14. The penalty parameter  $\lambda$ , following extensive numerical experimentation, is defined as the diagonal matrix,

$$\lambda^p \rightarrow [\lambda]^p \equiv C \Delta x [U1]_{j+1}^p \quad (19)$$

where  $C$  is a constant of order unity, and the elements (on the diagonal) of  $[U1]_{j+1}^p$  are  $\{U1\}_{j+1}^p$ , the nodal distribution of  $\{Q1\}$  computed at each iteration  $p$  at  $x_{j+1}$ .

The functional form of the penalty term, equation 13, involves definition of an auxiliary dependent variable  $\bar{\phi}^h$ , as

$$L(\bar{\phi}^h) = \frac{\partial}{\partial x_j} \left( \bar{\phi}^h \frac{\partial u_j^h}{\partial x_j} \right) \equiv \frac{\partial^2 \bar{\phi}^h}{\partial x_j^2} \quad (20)$$

The boundary conditions for  $\bar{\phi}$  are a linear combination of homogeneous Dirichlet and Neumann constraints, defined according to required flow porosity on various segments of  $\partial R$ . Hence,  $\bar{\phi}^h$  is augmented for one additional entry, the solution of

$$L(\bar{\phi}^h) = \frac{\partial^2 \bar{\phi}^h}{\partial x_j^2} - \frac{\partial(\bar{\phi}^h u_j^h)}{\partial x_j} = 0 \quad (21)$$

1005062886

The Galerkin weighted-residuals algorithm statement for equation 21 is the algebraic equation system  $(F13) = \{0\}$ , which is added to equation 13, hence equations 16-18. Therefore, the explicit form of the complete penalty term in equation 13 is:

$$\lambda \int_{R_2} \frac{\partial(N_1)}{\partial x_1} L(\phi^h) d\tau \quad (22)$$

$$\equiv \int_{R_2} \left[ C_{\lambda x} \int_{R_2} [U_1]_e \frac{\partial(N_1)}{\partial x_1} (N_1)^T \{e\}_e d\tau \right]$$

Regarding the Newton algorithm Jacobian, equation 18 is replaced with two sparse matrices, yielding a corresponding compromise on overall convergence rate while significantly reducing the matrix rank. The initial-valued dependent variables  $\{U\}_i, k_i, \epsilon_i$  are sequentially solved as multiple right side substitutions to equation 16, using the  $\bar{U}_1^j$  Jacobian,  $[J11]_j$ , where

$$[J11] \equiv \frac{\partial(F1)}{\partial(U1)} \quad (23)$$

The Poisson field variables  $\{\phi^h, \phi^h\}$  are solved sequentially as multiple right side substitutions using the  $\bar{U}_1^j$  Jacobian [366]. The scalar components of  $\bar{U}_1^j$  are determined using an elemental averaging and assembly procedure, equivalent to solving equation 16 using [377] for multiple right side substitutions. The algorithm timing utilizes the sequence [311], [366], [377], with update of the Jacobians occurring at every iteration. Details of the formation of these Jacobians is given in reference 7.

#### IV. Results and Discussion

##### Benchmark Tests

The PNS finite element penalty algorithm, as operational in the CMC3DPNS computer code, is well documented for subsonic aerodynamic problem definitions involving semi-bounded and fully bounded solution domains [1,11]. Additional documentation is reported [2] for an unbounded aerodynamic wake-type flow. Each of these includes detailed comparisons between algorithm prediction and experimental data, including the complete Reynolds stress tensor for two- and three-dimensional geometries. These comparisons serve to quantitatively verify the appropriateness of the "standard" turbulence model constants  $C_{\lambda}$ , equation 6, which are used for the free-jet analyses.

As the typical case in three-dimensional, turbulent aerodynamic flow prediction, quality experimental data to initiate solutions is usually non-existent. Hence, tests were conducted to evaluate self-generation of initial conditions for the free-jet configuration. The basic assumption was that the sole available initial data is the dominant velocity scalar component  $\bar{U}_1(x_1, x_2)$  on the PNS solution initiation plane. Figure 2 illustrates a two-dimensional slot jet test problem thus characterized by  $\bar{U}_1(x_1, x_2) \equiv U_1$ , within and exterior to the jet. Since a non-zero background level of dissipation function is a computational requirement ( $\epsilon^{-1}$  appears throughout equations 4-6), background levels of both  $k^0 > 0$  and  $\epsilon^0 > 0$  are defined to yield a background "turbulent viscosity" level  $\nu_t = C_{\lambda} k^2 / \epsilon$  of the order of the

laminar viscosity  $\nu$ . Numerical experimentation indicates  $k^0 = O(10^{-4})$  and  $\epsilon^0 = O(10^{-9})$  yield adequate algorithm stability. At the knee of the profile in  $\bar{U}_1$ , Figure 2, the initial level of turbulent viscosity is assumed known, e.g.,  $10 \leq \nu_t/\nu \leq 10^2$ . Since the nominal extremum order of  $k$  is  $O(10^{-2})$ , this can be achieved by setting  $k^0 = O(10^{-2})$  and  $\epsilon^0 = O(10^{-7})$ .

Figure 3 summarizes the PNS penalty algorithm prediction for the symmetric-half slot jet problem, for  $\bar{U}_1^{\text{lower}} \equiv 0.02 \bar{U}_1^{\text{jet}} \equiv \bar{U}_1^{\text{upper}}$  and  $\nu_t^0 = O(10^2)$ , on the span  $0 \leq x_1/H_1 \leq 1.0$ , where  $H_1$  is the slot jet half-width. The initial condition for  $\bar{U}_1$  was interpolated as a step function on the nodes of the discretization of  $x_2$ , yielding the spiked initial conditions for  $k^0$  and  $\epsilon^0$  shown as solid lines. The maximum levels of  $k$  and  $\epsilon$  increase by a factor of 2-4, by  $x_1/H_1 = 0.5$ , and thereafter decrease monotonically as the enhanced level of  $\nu_t$  diffuses into the velocity defect region. The jet potential core is eroded by about 23% by  $x_1/H_1 = 1.0$ .

Figure 3b) summarizes the entrainment action predicted by the penalty algorithm. By definition,  $\bar{U}_2 \equiv 0$ , as shown by the solid line. Since the order delta  $\bar{U}_2$  momentum equation is homogeneous, the sole source for  $\bar{U}_2 \neq 0$  is the action of the penalty constraint in equation 13. The PNS solution indicates a large entrainment at  $x_1/H_1 = 0.5$ , where  $\bar{U}_2 = -0.1$  in the farfield, which progressively moderates as the solution proceeds further downfield. The boundary conditions for  $\phi$  for this geometry are  $\phi = 0$  at the farfield and  $\partial\phi/\partial x_2 = 0$  on the symmetry line.

The second basic test is the three-dimensional problem of a single jet of initially circular cross-section. For this case,  $\bar{U}_{\text{jet}} = \bar{U}_1 (= 30 \text{ m/s})$  and  $\bar{U}_{\text{exterior}} = 0.1 \bar{U}_1$ . Figure 4 summarizes the PNS prediction of transverse half-plane velocity field at  $x_1/H_1 = 1.0$ , where  $H_1$  is the radius of the initial jet, for laminar flow and for turbulent flow with  $\nu_t^0 = 10$ . Both solutions exhibit the required symmetries and predict essentially radial entrainment. The plot length of each individual velocity vector is the measure of the relative magnitude of  $\bar{U}_1$ , scaled to the local predicted extremum magnitude  $\bar{U}_1^{\text{ext}}$ . For the laminar flow prediction,  $\bar{U}_1^{\text{ext}} = 0.0317$ , while  $\bar{U}_1^{\text{ext}} = 0.044$  for the turbulent case. Thus, the measure of magnitude of entrainment for the turbulent case is approximately 20 times that for the laminar case, in qualitative agreement with expected behavior. The boundary conditions for  $\phi$  for this case are  $\phi = 0$  everywhere in the farfield and  $\partial\phi/\partial x_2 = 0$  on the symmetry plane. As in the two-dimensional test,  $\bar{U}_2 \equiv 0$ , and the penalty term in equation 13 is the sole causal mechanism initiating and maintaining the computed transverse plane velocity field.

##### Multiple Free Jet PNS Prediction

The multiple jet case of main interest corresponds to a symmetric four-jet geometry with the jets located in close proximity and of small initial diameter. This configuration is verified, using experimental smoke flow visualization techniques, to rapidly induce a substantially large transverse plane velocity field which efficiently pumps fluid, initially interior to the circumference of the jets, into the exterior region. Figure 5a) illustrates the persistent unidirectional flow of smoke obtained with the multi-jet system inoperable. Figure 5b) shows the rapid smoke dispersal promoted by the multiple jet system operating at design conditions.

1005062887

Figure 6 is a layout sketch of the multiple jet device indicating characteristic dimensions. Operating on design, free air is induced to flow down each vent channel, of length 0.02 m, at a nominal velocity  $U_j = 12$  m/s. The locator radius of the jets is  $R = 0.004$  m, and the initial hydraulic diameter of each jet is  $d_j = 0.001$  m. In the region interior to  $R$ ,  $U_j = 0.02 U_\infty$  while in the essentially unbounded exterior region  $U_j = 0$ . The characteristic Reynolds number for the jet flow is  $Re = 10^6$  m, and the vent channel walls are quite rough.

The symmetry of this multiple jet geometry permits the majority of PNS calculations to be performed on the symmetric quarter domain with boundary OABC, Figure 6. Figure 7 graphs this domain showing the nodal coordinates of the basic  $M = 19 \times 19$  non-uniform computational mesh. The lateral extent of the domain spans twice the locator radius  $R$ . Segments OA and OB are symmetry planes, upon which the normal component of velocity vanishes and all other variables possess vanishing normal derivatives. Boundary segment ACB is assumed sufficiently remote, such that all dependent variables have vanishing normal derivatives except  $\theta$ , which vanishes identically since the boundary is porous.

For the basic assessment, the sole specified initial conditions are  $\bar{U}(x_1, x_2)$ , and the levels of  $\bar{v}_\theta$  in the air jet and background flows. Since the PNS predicted secondary vortex flow field develops very rapidly, a relatively large (20%) background  $\bar{U}_j$  velocity field was used for efficiency. (The PNS algorithm stability was marginal using a 10% background flow specification. Small, but not significant differences were predicted in  $\bar{U}_j(x_1, x_2)$  distributions at various stations downstream of the injector face. The assumed initial level of  $\bar{v}_\theta$  exerts a much more significant influence.) Therefore, within the air jet,  $\bar{U}_j = 1.2 U_\infty$ , where  $U_\infty = 12$  m/s, the design velocity. Everywhere exterior to the locator radius,  $\bar{U}_j = 0.2 U_\infty$ , and interior  $\bar{U}_j = (0.2 + 0.02) U_\infty$ . Hence, the  $\bar{U}_j$  velocity strain rate distribution on the initial surface plane was on-design. Further, within the air jet  $k^0 = 0.0025$ , with  $\epsilon^0$  defined such that  $\bar{v}_\theta/\bar{U}_j = 35$ . Everywhere exterior to the jet,  $k^0 = 0.0001$  and  $\bar{v}_\theta/\bar{U}_j = 3$ .

Figure 8 is a composite of the multiple vortex secondary velocity field predicted by the PNS algorithm at  $x_1/R = 1.5$ , i.e., 6 mm downstream from the plane of solution initiation. As in Figure 4, each velocity vector length is scaled to the extremum predicted level  $(\bar{U}_j/U_\infty)_{\max} = \bar{U}_j^0 = 0.067$ . The original location of each air jet coincides with the clustering of large radial velocities, and the net action of the four-jet device is to induce a system of eight symmetrically disposed, counter-rotating transverse vortex pairs. At this  $x_1$  station, the maximum axial velocity component within the initial jet region was  $\bar{U}_j = 0.35$ , hence the local ratio  $\bar{U}_j/\bar{U}_j^0 = 0.19$  is quite substantial in comparison to the PNS ordering analysis.

Quarter-plane plots of the PNS predicted evolution of the transverse plane vortex flowfield in the near vicinity of the locator radius and air jet are shown in Figure 9. A substantial field exists by  $x_1/R = 0.5$ , which is 2 mm downstream from the initial condition plane, although the vortex pattern has not matured. However, by  $x_1/R = 1.0$ , Figure 9b), the counterrotating pattern is clearly evident and  $\bar{U}_j^0 = 0.038$  has remained essentially constant. By  $x_1/R = 1.5$ , Figure 9c), the visual appearance of the  $\bar{U}_j$  distribution is nominally unchanged, although the overall strength has increased by about 15% since  $\bar{U}_j^0 = 0.067$ . The visual appearance

of the double counter-rotating vortex pattern shown in Figure 9c) persists essentially unchanged for distances up to  $x_1/R = 11$  downstream of the initial condition plane.

A species continuity equation, similar in appearance to equation 7, was added to the PNS system, to permit tracking of the distribution of fluid initially interior to the locator radius  $R$ . Figure 10a shows the  $Y^0 = 100\%$  smoke distribution at the solution initiation plane; the four troughs correspond to the location of the four air jets. Diffusion processes dominate on  $0 \leq x_1/R \leq 1$ , Figure 10b), and the extremum smoke concentration  $Y_m$  remains 100%. By  $x_1/R = 2.0$ ,  $Y_m = 97\%$ , at  $x_1/R = 3.0$   $Y_m = 84\%$ , and the first non-zero level  $Y_e$  occurs at the boundary  $\partial R$  of the PNS domain at  $x_1/R = 5.0$ , Figure 10c), where  $Y_m = 63\%$ . By  $x_1/R = 11.0$ ,  $Y_m$  has decreased to 30% and  $Y_e = 23\%$ , Figure 10d). Hence, the counter-rotating vortex system has homogenized the initial smoke level within a distance of about 44 mm. Of greatest significance, on  $\partial R$  at  $x_1/R = 11.0$ ,  $\partial Y/\partial x_1 \cdot \Delta x_1 > 0$  confirms that the material transport is dominated by convection, in qualitative agreement with the smoke flow visualization experimental data.

Figure 11 summarizes the PNS computed distribution of turbulent kinetic energy  $k(x_1)$  on  $0 \leq x_1/R \leq 1.5$ . The initial condition is  $k^0 = 0.0025$ , Figure 11a), within the jets and  $k^0 = 0.0001$  elsewhere. Due to the rapid decay of the air jets, the extremum level of  $k$  at  $x_1/R = 0.12$  has increased sharply to  $k_m = 0.022$ , Figure 11b). This has further increased to  $k_m = 0.035$  at  $x_1/R = 0.25$ , Figure 11c), and the crater shape of each profile is clearly evident. Diffusional processes eventually smooth the distributions, Figure 11d), and the extremum level has been reached,  $k_m = 0.039$ . Continuing downstream, the distributions of  $k$  become further homogenized at nominally the same maximum level.

A series of computational experiments were conducted to ascertain importance of assumed initial turbulence level on the PNS prediction. For one test,  $k^0$  was halved to  $k^0 = 0.00125$  and  $\epsilon^0$  held constant, yielding  $\bar{v}_\theta/\bar{U}_j = 9$ . A second test was conducted with the air jets assumed laminar. Figure 12 summarizes these predictions in terms of decay of the jet velocity extremum,  $\bar{U}_j(x_1)$ , and the extremum predicted vortex velocity component  $\bar{U}_j^0(x_1)$ . For the laminar flow case, the air jet extremum does not decrease at all on  $0 \leq x_1/R \leq 1.5$ , and the induced transverse plane component hovers about  $\bar{U}_j^0 = 0.01$ . In distinction, halving the initial turbulence level simply displaces the jet decay curve to the right, a distance of  $\Delta x_1/R = 0.25$ , and yields an extremum transverse component that is only modestly smaller by about  $\Delta \bar{U}_j^0 = 0.003$ . In comparison to the experimental data, these predictions confirm the importance of the vent channel roughness in promoting the desired action of the multi-jet system. In the same sense, the assumed initial level for  $k^0$  does not appear critical, in terms of the PNS solution, predicting a qualitatively valid solution, provided  $\bar{v}_\theta$  is sufficiently large to permit self-generation of solutions to the  $k$ - $\epsilon$  equation system.

Additional experimental data confirms that sufficient protrusion of the locator radius surface beyond the multi-jet injector face can markedly reduce the level of visually apparent swirling motion. This geometry modification was modeled by assuming the locator radius  $R$ , Figure 7, was a solid surface for a specified distance  $\Delta x_1/R$  downstream. Hence, the initial PNS solution domain is contained within the radius surface, and the boundary conditions on this surface are  $\bar{q}_n = (0)$ . After marching the prescribed distance, the PNS solution is



stopped, the locator radius surface is computationally removed and the remainder of the solution domain OABC added, and the PNS solution restarted using the current solution as initial conditions.

Figure 13 summarizes the resulting PNS prediction of  $\bar{u}(x_1, x_2)$ . Since the solid locator radius surface is a sink for momentum, one expects that a proportionally larger level of transverse plane velocity will result. Figure 13a) confirms this for a 1 mm extension. The nominally radial flow from the jet region is evident, it does not penetrate the radius boundary, and  $u_m^* = 0.182$  is more than double the extremum predicted without the extension. Figure 13b) shows the  $\bar{u}_y$  distribution computed at  $x_1/R = 0.75$  with the solid surface appended. A weak vortex pair is barely discernable, and  $u_m^* = 0.052$  has decayed by a factor of three. Figure 13c) shows the  $\bar{u}_y$  distribution computed at  $x_1/R = 1.5$ , downstream of the 1 mm extension, which used the data of Figure 13a) as initial conditions. Comparing to the on-design solution, Figure 9c), a single vortex pair of much weaker strength has replaced the basic prediction. Even though the extremum of  $u_m^* = 0.055$  is only modestly decreased, the vortex pattern of Figure 13c) would be much less effective in promoting convection of material from within the interior region.

For a final computational experiment, the available smoke flow visualization data indicate that the multiple jet device efficiency is only modestly altered by partial blocking of one of the initial jets. Since this constraint destroys the inherent geometric symmetries, the PNS solution domain must now encompass a region that is a factor of four larger. Figure 14 graphs the transverse velocity distribution  $\bar{u}_y$  at  $x_1/R = 1.5$  on an  $M = 19 \times 19$  mesh that is twice as coarse as the base discretization, Figure 7. However, comparing Figure 8 and 14 confirms that the coarse grid full solution has captured the essential eight-vortex pair structure, and  $u_m^* = 0.034$  is within 20% of the finer grid extremum, Figure 9c).

Figure 15 graphs the PNS predicted transverse plane velocity distribution  $\bar{u}_y$  at  $x_1/R = 1.5$  obtained with the lower right jet completely shut off. A through-flow has resulted over the occluded jet, and the extremum level of  $u_m^* = 0.12$  is about 50% larger than the design configuration. Figure 16 compares the computed distributions of smoke density at  $x_1/R = 6.0$  for both coarse grid solutions. Figure 16a) compares visually with the finer grid solution, Figure 10c), and  $Y_m = 53\%$  lies on the interpolation of trajectory extremum. The loss action of the occluded vent is clearly evident in Figure 16b), although  $Y_m = 59\%$  is only 10% larger than the on-design solution. These PNS predictions thus agree qualitatively with the field data, and further permit a quantitative comparison measure of the action of design modifications.

#### V. Conclusions

The finite element penalty numerical solution algorithm for the three-dimensional parabolic Navier-Stokes equations, for subsonic turbulent flows, has been applied to prediction of secondary vortex flowfields induced by multiple free-jets issuing in close proximity. The combined action of rapid jet decay and discreteness of the multiple jet configuration has been quantitatively assessed regarding resultant entrainment and secondary vortex structures. No detailed experimental measurements are available for comparison of the numerical predictions. However, interpretation of inexpensively acquired video-graphic smoke flow

visualization data has provided a basis for qualitative comparisons. Further, a range of computational experiments were conducted, involving parameter variations, that permitted further qualitative comparisons. The availability of the computer program embodiment of the theory, as a computational laboratory, has been verified of utility and of sufficient versatility to permit a range of experiments. It is fair to assume that this constitutes one small step towards the eventual realization of computational fluid dynamics as a diagnostic practice.

#### VI. References

1. Baker, A. J., and Orzechowski, J. A., "An Interaction Algorithm For Three-Dimensional Turbulent Subsonic Aerodynamic Junction Region Flow," AIAA J., V. 21, 1983, to appear.
2. Dodge, P. R. and Lieber, L. S., "A Numerical Method For the Solution of Navier-Stokes Equation For a Separated Flow," Technical Paper AIAA-77-170, 1977.
3. Patankar, S. V., *Numerical Heat Transfer and Fluid Flow*, McGraw-Hill/Hemisphere, NY, 1980.
4. Briley, W. R., and McDonald, H., "Analysis and Computation of Viscous Subsonic Primary and Secondary Flows," Technical Paper AIAA-79-1453, 1979.
5. Mikhail, A. G. and Ghia, K. N., "Analysis and Asymptotic Solutions of Compressible Turbulent Corner Flow," Trans. ASME, J. Engr. Power, V. 104, 1982, pp. 571-579.
6. Cebeci, T., and Smith, A.M.O., *Analysis of Turbulent Boundary Layers*, Academic Press, New York, 1974.
7. Baker, A. J., *Finite Element Computational Fluid Mechanics*, McGraw-Hill/Hemisphere, NY, 1983.
8. Baker, A. J., "The CMC:3DPNS Computer Program For Prediction of Three-Dimensional, Subsonic, Turbulent Aerodynamic Junction Region Flow - Volume I - Theoretical," NASA Technical Report CR-165997, 1982.
9. Manhardt, P. D., "The CMC:3DPNS Computer Program For Prediction of Three-Dimensional, Subsonic, Turbulent Aerodynamic Junction Region Flow - Volume II - User's Manual," NASA Technical Report CR-165997, 1982.
10. Orzechowski, J. A., "The CMC:3DPNS Computer Program For Prediction of Three-Dimensional, Subsonic, Turbulent Aerodynamic Junction Region Flow - Volume III - Programmer's Manual," NASA Report CR-165998, 1982.
11. Baker, A. J., and Orzechowski, J. A., "A Continuity-Constrained Finite Element Algorithm For Three-Dimensional Parabolic Flow Prediction," Proceedings ASME Sym. on Computers in Flow and Experiments, ASME/WAM, 1982, pp. 103-117.
12. Baker, A. J., Yu, J. C., Orzechowski, J. A., and Gatski, T. B., "Prediction And Measurement of Incompressible Turbulent Aerodynamic Trailing Edge Flows," AIAA Journal, V. 22, No. 1, 1982, pp. 32-37.

1005062889

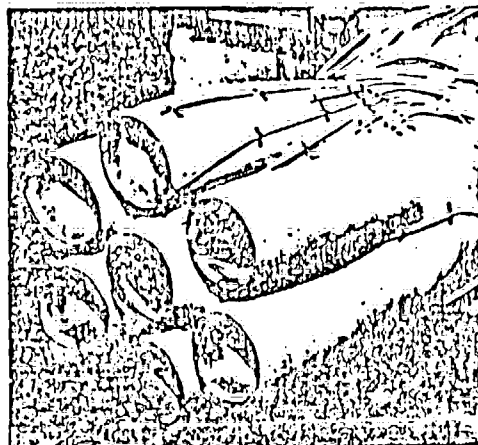


Figure 1. Illustration of a Multiple Jet Configuration.

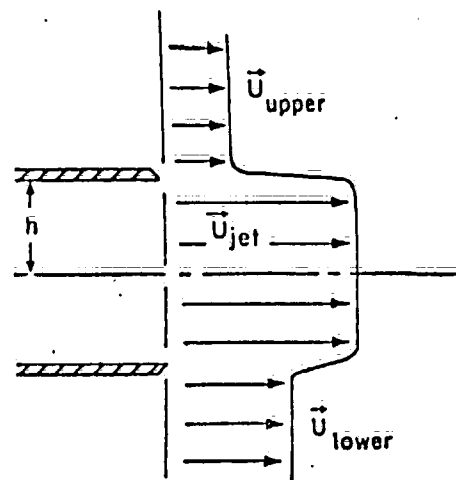
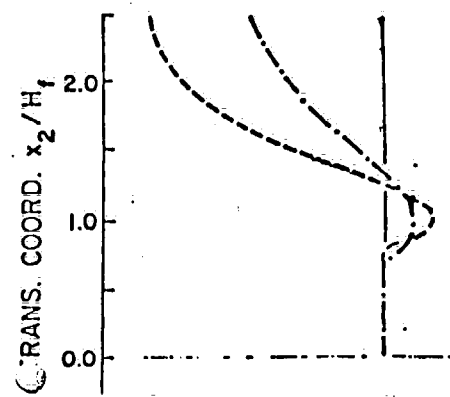
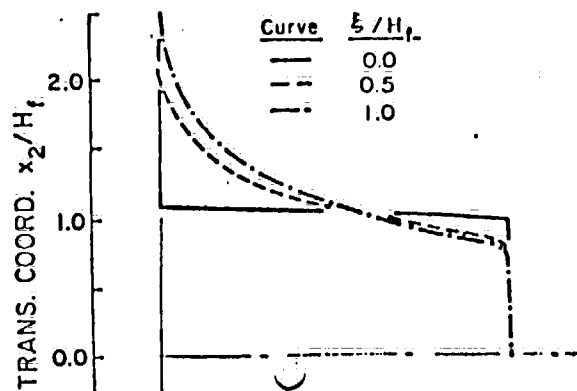


Figure 2. Geometry of a Two-Dimensional Slot Jet.



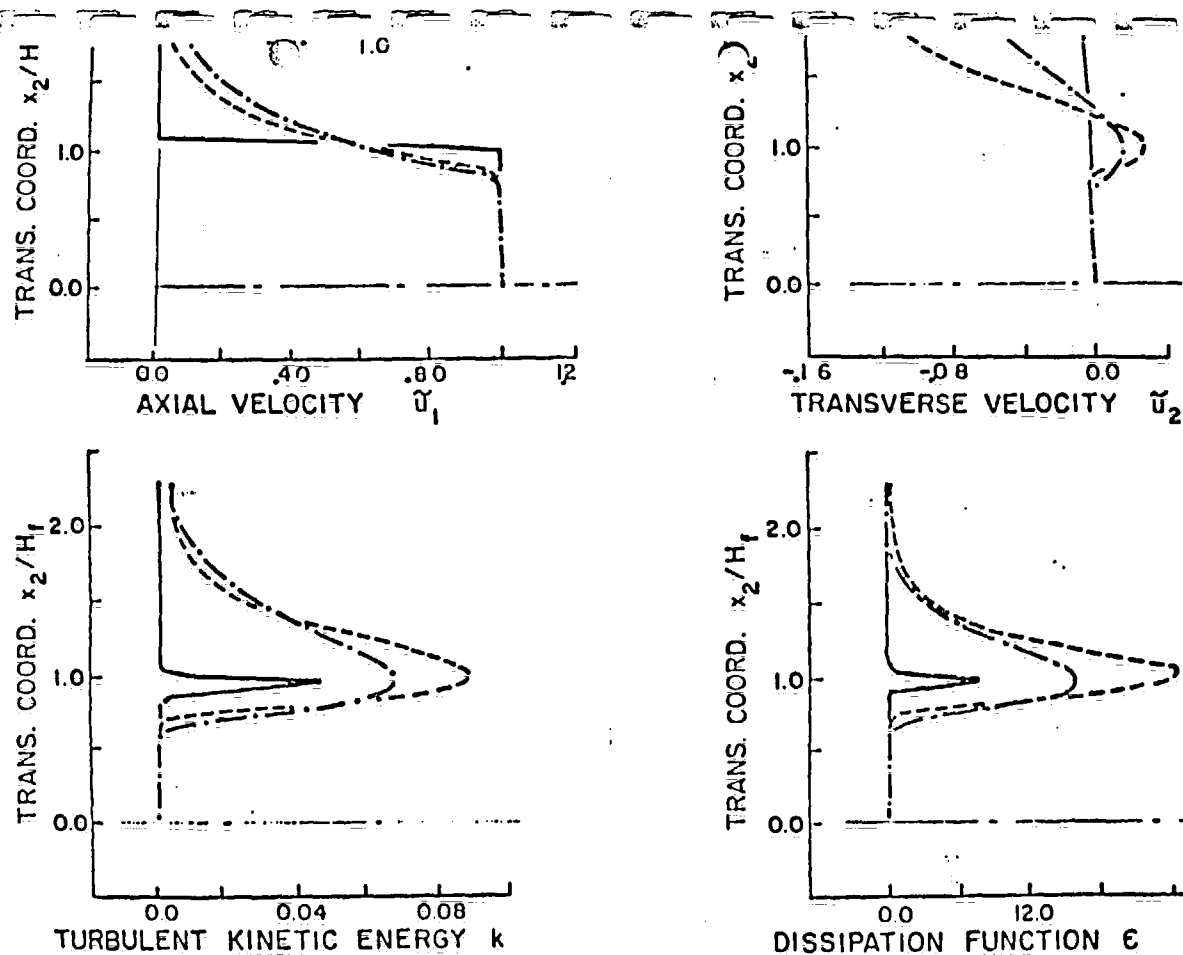


Figure 3. Penalty Algorithm Solution of Symmetric-Half Subsonic Slot Jet,  $\bar{u}_1^0 = 30$  m/s,  $0 \leq x_1/H_1 \leq 1.0$ , a) Axial Mean Velocity  $\bar{u}_1$ , b) Transverse Mean Velocity  $\bar{u}_2$ , c) Turbulent Kinetic Energy  $k$ , d) Isotropic Dissipation Function  $\epsilon$ .

1005062891

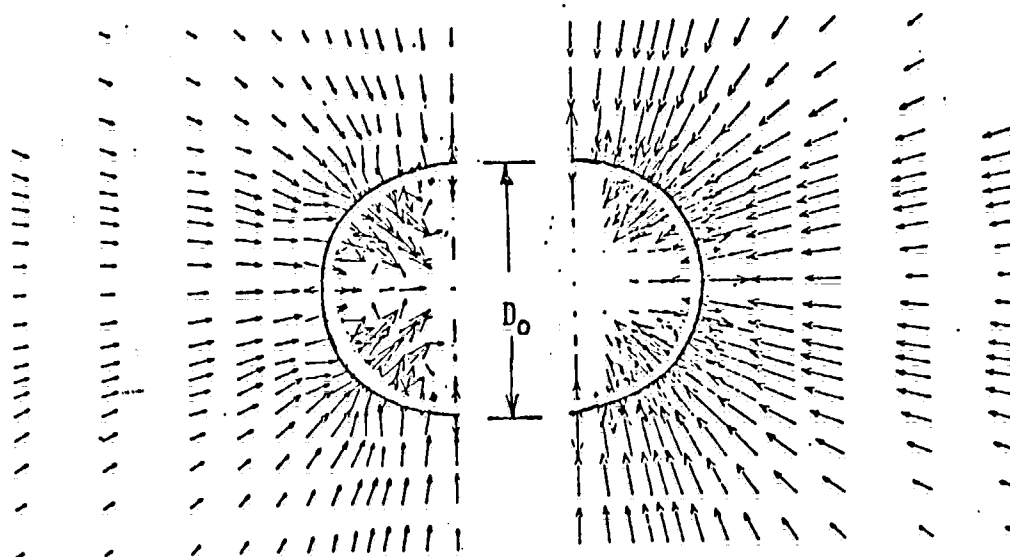


Figure 4. Penalty Algorithm Solution For Transverse Mean Velocity  $\bar{u}_y$  Distribution, Symmetric-Half Circular Free Jet,  $\bar{u}_1 = 30$  m/s,  $x_1/D_h = 1.0$ , a) Laminar Jet,  $u_1^0 = 0.0017$ , b) Turbulent Jet,  $u_1^0 = 0.044$ .

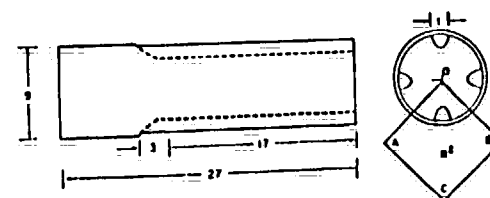
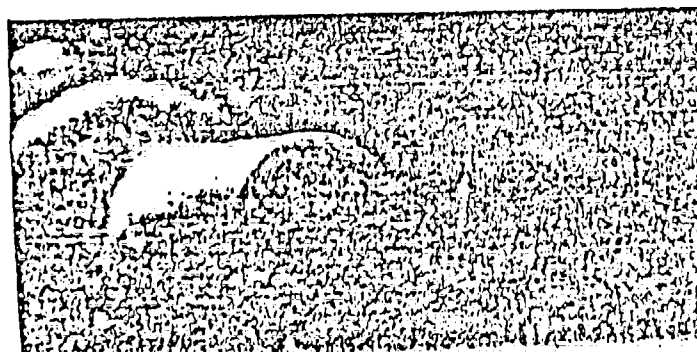


Figure 6. Engineering Layout of Multiple Jet

1005062892

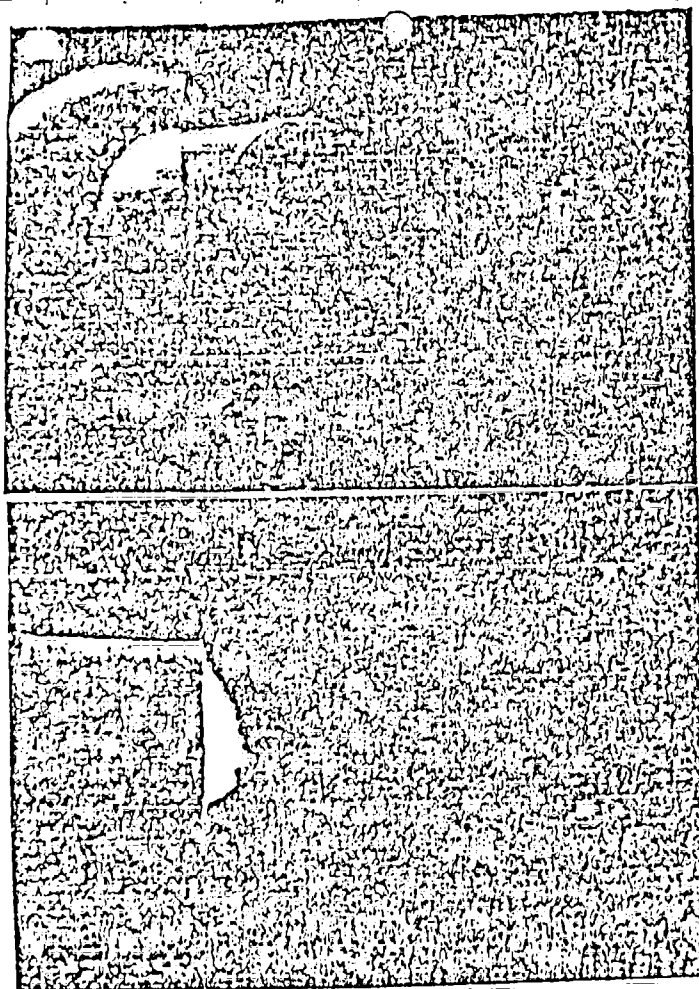


Figure 5. Smoke Flow Visualization of Multiple-Jet Configuration, a) Jet Flows Off, b) Jet Flows On.

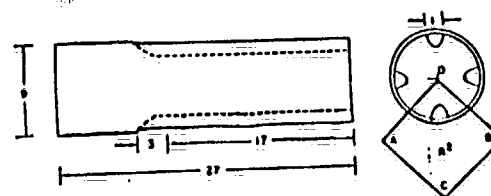


Figure 6. Engineering Layout of Multiple Jet Geometry, a) Plan-View, b) End View, Dimensions in mm.

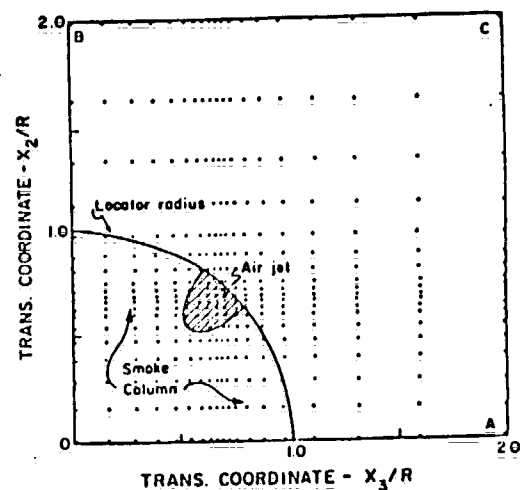


Figure 7. Penalty Algorithm Solution Domain For Symmetric Quarter Plane Prediction of Four Multiple Jet Configuration Including Nodal Coordinate Distribution of  $M = 19 \times 19$  Discretization.

1005062893

1005062894

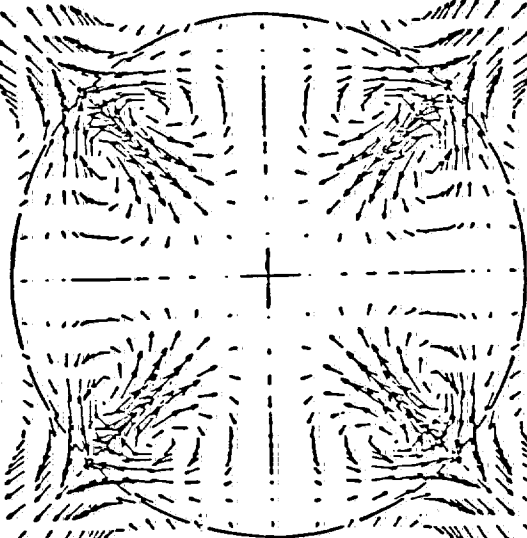


Figure 8. Composite Penalty Algorithm Prediction of Transverse Plane Velocity  $\bar{u}_y$  Distribution, Four Multiple Jet Geometry,  $\bar{u}_1 = 12$  m/s,  $x_1/R = 1.5$ .

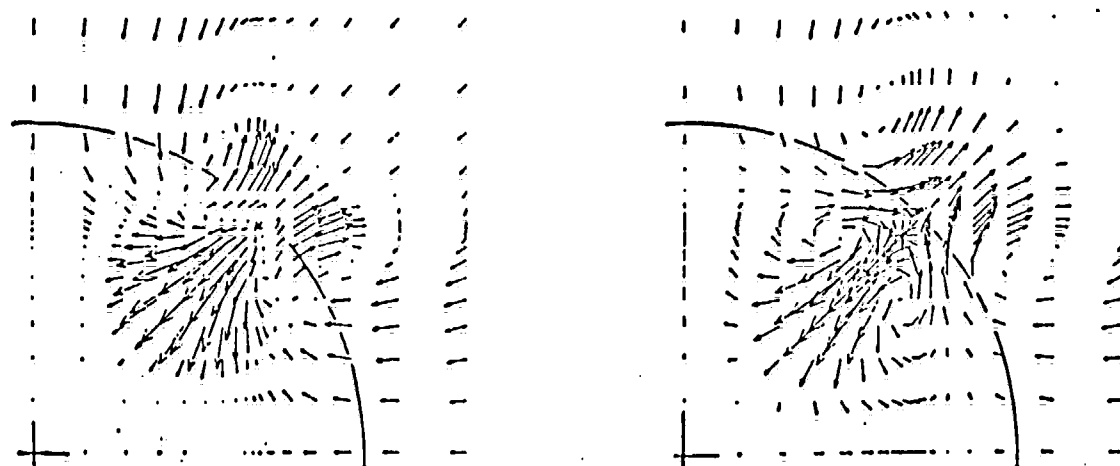


Figure 9. Nearfield Transverse Plane Velocity  $u_y$  Distributions, Penalty Algorithm Prediction,  $\bar{u}_1^0 = 12$  m/s, a)  $x_1/R = 0.5$ ,  $u_1^0 = 0.058$ , b)  $x_1/R = 1.0$ ,  $u_1^0 = 0.058$ , c)  $x_1/R = 1.5$ ,  $u_1^0 = 0.067$ .

1005062895

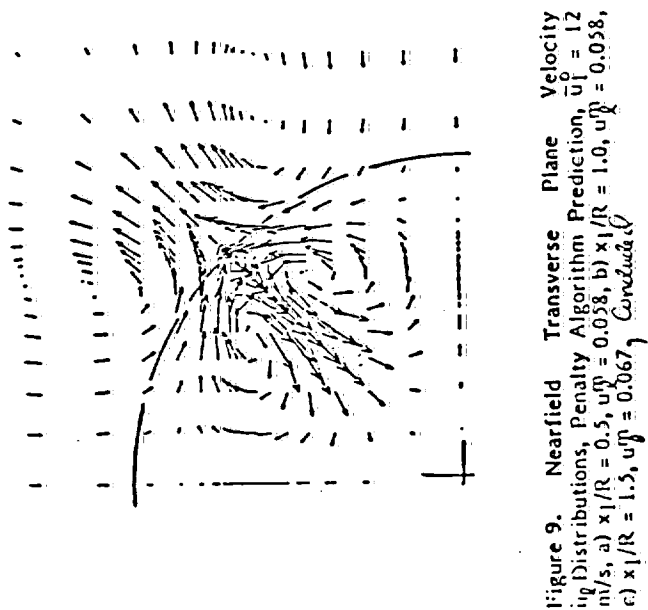


Figure 9. Nearfield Transverse Plane Velocity Visualization, Penalty Algorithm Prediction,  $u_1^0 = 12$  m/s, a)  $x_1/R = 0.5$ ,  $u_1^0 = 0.058$ , b)  $x_1/R = 1.0$ ,  $u_1^0 = 0.058$ , c)  $x_1/R = 1.5$ ,  $u_1^0 = 0.067$ ,  $Y_m = 0.5\%$ .

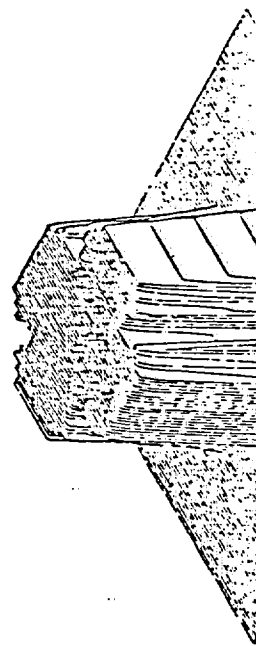
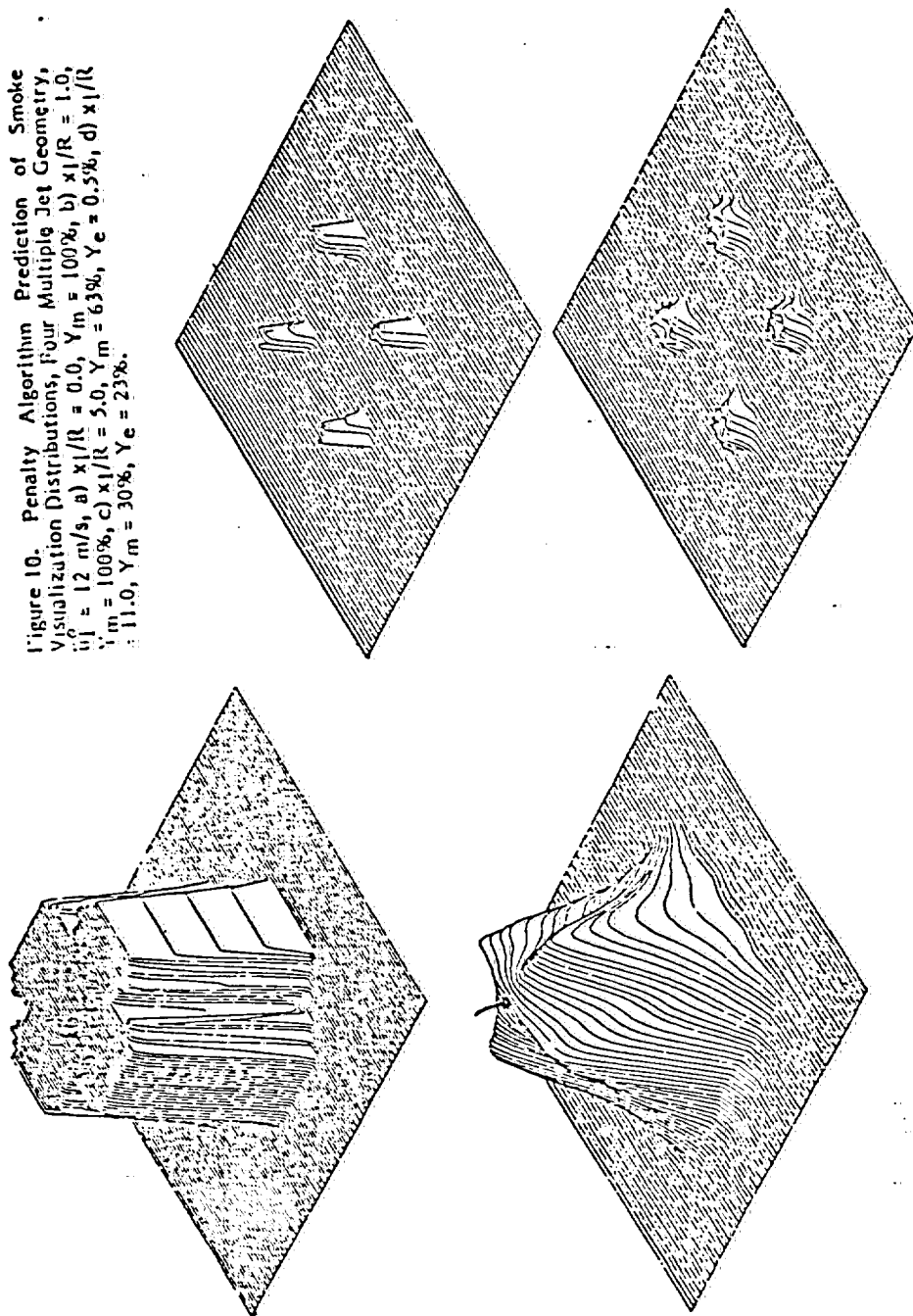


Figure 10. Penalty Algorithm Prediction of Smoke Visualization Distributions, Four Multiple Jet Geometry,  $u_1^0 = 12$  m/s, a)  $x_1/R = 0.0$ ,  $Y_m = 100\%$ , b)  $x_1/R = 1.0$ ,  $Y_m = 100\%$ , c)  $x_1/R = 5.0$ ,  $Y_m = 63\%$ ,  $Y_c = 0.5\%$ , d)  $x_1/R = 11.0$ ,  $Y_m = 30\%$ ,  $Y_c = 23\%$ .

1005062896



Figure 10. Penalty Algorithm Prediction of Smoke Visualization Distributions, Four Multiple Jet Geometry,  $u_0 = 12$  m/s, a)  $x_1/R = 0.0$ ,  $Y_m = 100\%$ , b)  $x_1/R = 1.0$ ,  $Y_m = 100\%$ , c)  $x_1/R = 5.0$ ,  $Y_m = 63\%$ ,  $Y_e = 0.5\%$ , d)  $x_1/R = 11.0$ ,  $Y_m = 30\%$ ,  $Y_e = 23\%$ .



1005062897